

# Aircraft-derived particle fluxes distinguish entrainment zone and decoupled layer nucleation in marine boundary layers

Ajmal Rasheeda Satheesh<sup>1</sup>, Markus D. Petters<sup>2</sup>, and Nicholas Meskhidze<sup>1</sup>

<sup>1</sup>Department of Marine, Earth, and Atmospheric Sciences, North Carolina State University, Raleigh, NC 27695, USA.

<sup>2</sup>Department of Chemical and Environmental Engineering, University of California, Riverside, CA 92521, USA.

Corresponding author: Nicholas Meskhidze (nmeskhidze@ncsu.edu)

## Abstract

The vertical distribution of freshly nucleated aerosol particles in the marine boundary layer remains poorly constrained, limiting our ability to represent new particle formation in climate models. Here we characterize 3–10 nm particle events, termed small particle events (SPEs), by deriving their vertical turbulent fluxes from aircraft measurements during the Aerosol and Cloud Experiments in the Eastern North Atlantic (ACE-ENA) campaign. To overcome stationarity limitations of traditional eddy covariance methods, we applied continuous wavelet transform analysis to data collected during June–July 2017 and January–February 2018 flights over the Azores. Our flux-based analysis revealed two distinct SPE scenarios with different vertical structures and spatial extents. The first featured nucleation in the entrainment zone, where free tropospheric air entrains into the boundary layer. The second showed nucleation in the decoupled layer, a stratified region between the well-mixed surface layer and cloud-topped upper boundary layer. In both cases, convergence of air masses from different layers diluted preexisting aerosol surface area to very low levels, creating conditions favorable for nucleation and generating strong downward particle fluxes. SPEs occurred in 15% of flights, challenging prevailing theoretical expectations that new particle formation should rarely occur in marine boundary layers due to high condensation and coagulation sink capacity of sea spray aerosols. Aircraft-derived particle fluxes provide first observational constraints on the vertical location and source strength of likely nucleation regions in the remote marine boundary layer, improving aerosol source representations in climate models and reducing uncertainties in aerosol-cloud interactions.

## 1. Introduction

Cloud adjustments due to aerosols constitute one of the most significant uncertainties in climate modeling (Intergovernmental Panel on Climate Change (IPCC), 2023). The magnitude of anthropogenic aerosol radiative forcing over the industrial period is strongly influenced by the abundance and properties of natural aerosols (Andreae, 2007; Carslaw et al., 2013; Hoose et al., 2009; Meskhidze et al., 2011). While uncertainties in aerosol radiative forcing from different processes (emissions, long-range transport, new particle formation, and removal) vary spatially, marine boundary layer (MBL) cloud microphysical properties exhibit the highest sensitivity to aerosol changes (Bellouin et al., 2020; Zhang et al., 2024). Understanding how marine low level clouds and their radiative effects respond to changing aerosol load is important due to their extensive spatial coverage, low optical thickness, and low background cloud condensation nuclei (CCN) concentrations. The response of these clouds to changes in aerosol loading remains

Formatted: Font color: Blue

Formatted: Font: Not Bold

Formatted: Font: Not Bold

Formatted: Font: Not Bold

Formatted: Font: Not Bold

Formatted: Font: Not Bold

Formatted: Font: Not Bold

Formatted: Font: Not Bold

Formatted: Font: Not Bold

Formatted: Font: Not Bold

Formatted: Font: Not Bold

Formatted: Font: Not Bold

Formatted: Font: Not Bold

**Deleted:** Abstract New particle formation (NPF) in marine boundary layers plays a critical role in cloud condensation nuclei (CCN) budgets and aerosol–cloud interactions, yet the vertical distribution of NPF sources, critical for predicting CCN production efficiency, remains poorly constrained. We identified the vertical location of NPF events by deriving turbulent fluxes of 3–10 nm particles from aircraft measurements during the Aerosol and Cloud Experiments in the Eastern North Atlantic (ACE-ENA) campaign. To overcome stationarity limitations of traditional eddy covariance methods, we applied continuous wavelet transform analysis to data collected during June–July 2017 and January–February 2018 flights over the Azores. Our flux-based analysis revealed two distinct NPF scenarios with fundamentally different vertical structures and spatial extents. The first scenario featured nucleation in the entrainment zone, where free tropospheric air entrains into the boundary layer. The second scenario showed nucleation in the decoupled layer, a stratified region between the well-mixed surface layer and cloud-topped upper boundary layer. Both cases exhibited strong downward particle fluxes driven by similar mechanisms: air masses meeting from different layers and mixing, which diluted aerosols to very low total particle surface area, creating favorable nucleation conditions. NPF occurred in 15% of flights, challenging prevailing theoretical expectations that NPF should rarely occur in marine boundary layers due to high condensation and coagulation sinks from sea spray aerosols. Aircraft-derived aerosol fluxes provide essential observational constraints on the vertical distribution and source strength of new particle formation in marine environments, enabling improved representation of these processes in climate models.<sup>4</sup>

62 poorly constrained and represents a key source of uncertainty in climate projections (Zhang et al., 2024).  
63 Consequently, understanding aerosol composition, dynamics, and the mechanisms controlling CCN number budgets  
64 within the MBL is critical for improving climate models and reducing predictive uncertainties. While freshly nucleated  
65 particles in the 3–10 nm size range must undergo substantial growth before reaching CCN-relevant sizes (>50–80  
66 nm), this growth pathway is well established in marine environments. At typical marine boundary layer growth rates  
67 of 1–3 nm hr<sup>-1</sup> (Ehn et al., 2010; Nieminen et al., 2018; O’Dowd et al., 2010; Zheng et al., 2018), newly formed  
68 particles can reach CCN sizes within 24–48 hours. This timescale is consistent with air mass residence times in the  
69 remote marine boundary layer (Kulmala et al., 2012; Zheng et al., 2021). Constraining the vertical location and flux  
70 magnitude of freshly nucleated particles therefore represents a critical first step toward understanding the full aerosol  
71 number budget in marine environments, including the ultimate contribution of NPF to CCN populations.

Formatted: Font color: Blue

72 Previous studies have identified three primary aerosol sources in remote MBLs: (1) long-range continental transport  
73 (Logan et al., 2014), (2) downward mixing of particles formed in the free troposphere (FT) through new particle  
74 formation (NPF) mechanisms (Clarke et al., 2013), and (3) sea spray emissions (Quinn et al., 2017). NPF occurring  
75 either near the top of stratocumulus cloud decks within open-cell regions (Petters et al., 2006) or in the upper portions  
76 of mid-latitude MBLs (Zheng et al., 2021), has been suggested as an important in-situ aerosol source within the MBL.

Deleted: (Zheng et al., 2021)

77 However, the difficulty in capturing actual nucleation events and determining their precise vertical location has led to  
78 the prevailing theoretical view that NPF should rarely occur in remote marine boundary layers over open oceans. This  
79 expectation is based on the high condensation and coagulation sink capacity of the remote MBL, which includes not  
80 only sea spray aerosols (Bates et al., 1998; Pirjola et al., 2000) but also accumulation-mode sulfate and organic  
81 particles entrained from the free troposphere (Yoon and Brimblecombe, 2002). Clouds further suppress NPF by  
82 scavenging Aitken-mode particles (Zheng et al., 2018), accelerating sulfate production on existing droplets through  
83 aqueous-phase SO<sub>2</sub> oxidation (Sanchez et al., 2021), and sequestering DMS oxidation products such as  
84 Hydroperoxymethyl thioformate (HPMTF) that would otherwise contribute to sulfuric acid formation (Novak et al.,  
85 2021). Independent corroboration of in-situ NPF over the eastern North Atlantic comes from the Azores  
86 Stratocumulus Measurements of Radiation, Turbulence and Aerosols (ACORES) campaign, which conducted  
87 helicopter-borne observations over Graciosa Island in July 2017, overlapping in time and location with the ACE-ENA  
88 campaign analyzed here. Siebert et al., (2021) reported frequent burst-like freshly nucleated particle events near the  
89 stratocumulus cloud top and in the free troposphere, while also noting that these particles did not grow to CCN-  
90 relevant sizes within the ~2-hour observation window. This outcome is expected given the 24–48 hour growth  
91 timescales discussed above. These concentration-based observations, however, could not determine the precise  
92 vertical location of the nucleation source regions, motivating the flux-based approach developed in the present study.

Moved (insertion) [1]

Moved up [1]: (Bates et al., 1998; Pirjola et al., 2000).

Deleted: This expectation is based on the relatively high surface area of sea spray aerosols, which act as condensation and coagulation sinks for nucleating vapors and newly formed particles

Deleted:

Formatted: Font color: Blue

Deleted: ¶

93 Determining the vertical origin of freshly nucleated particles, whether from the free troposphere, the interfacial layer  
94 near the marine boundary layer–free troposphere boundary, or the interface between the well-mixed marine boundary  
95 layer and decoupled layer, has critical implications for both fundamental understanding and climate modeling.  
96 Knowledge of where nucleation occurs is essential for understanding aerosol formation mechanisms and enabling  
97 climate models to accurately simulate aerosol number size distributions required for radiative calculations. Most  
98 atmospheric models have historically assumed that nucleation should be negligible in marine boundary layers, instead

106 predicting that particle formation would be favored at high altitudes where both temperature and aerosol surface area  
107 are substantially lower. However, traditional time-averaged aerosol concentration measurements from aircraft  
108 campaigns provide limited information about the precise vertical location where nucleation events occur. This  
109 limitation has prevented definitive identification of nucleation zones within the marine boundary layer and hampered  
110 efforts to constrain the relative importance of different aerosol sources to marine aerosol budgets. Without direct  
111 observational evidence of where particles form, climate models continue to rely on theoretical assumptions that may  
112 not accurately represent actual nucleation processes in marine environments.

113 To address this critical knowledge gap, vertical turbulent flux measurements of freshly nucleated 3–10 nm particles  
114 have emerged as particularly valuable tools for inferring the vertical location of likely nucleation source regions (Islam  
115 et al., 2022). The flux direction provides indirect evidence of the likely nucleation location; positive (upward) fluxes  
116 indicate nucleation below the aircraft, while negative (downward) fluxes suggest nucleation above the aircraft. This  
117 approach offers unprecedented spatial and temporal resolution for identifying nucleation zones that cannot be detected  
118 through conventional concentration measurements alone. In this study, we derive vertical turbulent fluxes of 3–10 nm  
119 particles using data collected during the Aerosol and Cloud Experiments in the Eastern North Atlantic (ACE-ENA)  
120 campaign. The campaign comprised two intensive operational periods (IOPs) – summer 2017 and winter 2018 –  
121 utilizing the G1 research aircraft from the DOE Atmospheric Radiation Measurement (ARM) program. By applying  
122 continuous wavelet transform techniques to high-frequency aircraft measurements, we provide the first flux-based  
123 observational constraints on the vertical distribution of likely NPF source regions in remote marine boundary layers,  
124 enabling improved representation of aerosol sources in climate models.

## 125 2. Materials and Methods

### 126 2.1 Sampling Site

127 The Department of Energy Atmospheric Radiation Measurement (DOE–ARM) Eastern North Atlantic (ENA) facility  
128 is positioned on Graciosa Island within the Azores archipelago, located in the northeastern Atlantic Ocean to the west  
129 of Portugal (Mather and Voyles, 2013). Air mass transport to this location follows four main pathways: (1) polluted  
130 outflow from North American sources, (2) continental emissions originating from northern European regions, (3)  
131 relatively clean Arctic air masses, and (4) air masses that recirculate within the Azores High pressure system (Wood  
132 et al., 2015; Zheng et al., 2018). The location is characterized by a low average annual aerosol optical depth (AOD)  
133 of 0.12 (Logan et al., 2014).

134 Data collection for this research occurred during the ACE-ENA field campaign, which included two intensive  
135 observation periods (IOPs): the initial period ran from June 21 to July 20, 2017, while the second period extended  
136 from January 15 to February 18, 2018 (Wang et al., 2019). All data from the ARM ENA site are publicly accessible  
137 through the ARM Data Discovery tool.

**Deleted:** CCN

**Formatted:** Font color: Blue

**Deleted:** vertical turbulent flux measurements of freshly nucleated particles have emerged as particularly valuable tools for characterizing the vertical location of particle nucleation

**Deleted:** The flux direction provides direct evidence of nucleation location...

**Deleted:** we provide the first direct observational constraints on the vertical distribution of new particle formation

146 **2.2 Instrumentation**

147 This study utilized datasets from the ARM Aerial Facility (Schmid et al., 2014). The G-1 research aircraft was  
148 equipped with over 50 instruments for comprehensive measurements of aerosols, clouds, and atmospheric processes.  
149 Detailed information regarding flight patterns executed during the campaign can be found in (Wang et al., 2019).  
150 Two Condensation Particle Counters (CPCs, models 3025A and 3772, TSI Inc.) with nominal 50% counting efficiency  
151 cutoff diameters of 3 nm and 10 nm, respectively, sampled through an isokinetic inlet exhibiting >90% efficiency for  
152 particles with aerodynamic diameters below 5  $\mu\text{m}$ . The concentration of 3–10 nm sized particles was calculated as the  
153 difference between these CPC measurements and is denoted as  $N_{3-10}$  throughout this paper. Since the measurements  
154 did not extend to particle sizes small enough to directly identify nucleation events, we follow (Islam et al., 2022) in  
155 using the term "small particle event" (SPE) to characterize these observations. The CPC 3772 operated at a constant  
156 1 LPM flow rate maintained by an external pump and critical orifice (Fan and Pekour, 2018), while the CPC 3025A  
157 sample flow rate was not actively controlled. Both flow rates remained stable across the sampling altitude range  
158 (Zheng et al., 2021). The airborne CPC configuration was validated for operation up to 4000 m altitude and across  
159 ambient relative humidity conditions of 0–90% RH. For a typical polluted environment ( $\sim 5000 \text{ cm}^{-3}$ ), CPC  
160 concentration measurements had an accuracy of 0.3 % (Kuang and Mei, 2019). All data used in this study passed  
161 instrument mentor specified quality control filters, which are distributed alongside the data.

162 Vertical wind speed ( $w$ ) was measured using the Aircraft Integrated Meteorological Measurement System probe  
163 (AIMMS-20, Aventech Research Inc.). The raw measurements define downward movement as positive; therefore,  
164 the sign was inverted to align with meteorological convention (positive values indicating updrafts and negative values  
165 indicating downdrafts). Although measurements were recorded at 20 Hz, they were downsampled to 1 Hz to match  
166 the temporal resolution of the CPC data acquisition.

167 Aerosol size distributions from 10 nm to 600 nm were characterized using a Fast Integrated Mobility Spectrometer  
168 (FIMS) (Kulkarni and Wang, 2006a, b). The FIMS provides size distribution measurements at 1-second temporal  
169 resolution with signal-to-noise characteristics, given by  $\sqrt{C}$ , where C is the number of particle counts detected in the  
170 corresponding size bin (Kulkarni and Wang, 2006a), suitable for detecting both remote continental and clean marine  
171 aerosol concentrations, as demonstrated in aircraft-based deployments (Kulkarni and Wang, 2006a, b; Olfert et al.,  
172 2008). Particles are charged within the instrument and separated by electrical mobility using an applied electric field.

173 The separated particles are subsequently grown into supermicron droplets in a condenser and imaged with a high-  
174 speed camera. This approach enables the FIMS to deliver size distribution measurements comparable to those of  
175 Scanning Mobility Particle Sizers (SMPS), but at a significantly higher time resolution. This study employed an  
176 advanced FIMS configuration utilizing a spatially varying electric field that extends the measurement range from 10  
177 nm to 600 nm (Wang et al., 2017b, a). Size distribution measurements were normalized to dry conditions; therefore,  
178 reported size distributions and number concentrations do not represent ambient humidity conditions. Cloud  
179 contamination filters were applied to prevent misclassification of cloud droplets as aerosol particles, with detailed  
180 filtering procedures described in the following section. FIMS-derived number concentration also served as a quality  
181 control flag for the CPC 3772. Since both instruments share an overlapping detection size range (10–600 nm for FIMS;  
182 >10 nm for CPC 3772), their total number concentrations should be broadly comparable (with CPC showing a higher

Deleted: -

Deleted: 1

Deleted:

Deleted: The FIMS provides high temporal resolution measurements with excellent sensitivity and counting statistics required for aircraft-based studies (Olfert et al., 2008)

189 total number concentration than FIMS) under a laboratory setting where all the variables are controlled. But the CPC  
190 concentration was found to be suspect at times, likely because of issues with the working fluid, or a change in flow  
191 rate that is controlled using a critical orifice. Hence, an arbitrary yet conservative threshold was set with CPC  
192 concentrations falling below 10% of the simultaneously measured FIMS concentration, indicating a physically  
193 implausible discrepancy inconsistent with real atmospheric variability, and were therefore excluded from analysis as  
194 likely instrument malfunctions.  
195 A two-dimensional stereo probe (2D-S) was used to retrieve drizzle concentration. It uses shadowgraphy to measure  
196 size distribution of hydrometeor particles in the size range 15  $\mu\text{m}$  to 2.5 mm (Glienke and Mei, 2019). All data  
197 products are publicly available through the ARM DOE website with citations in the data availability section and have  
198 undergone quality control by instrument mentors. Additional technical details are available in the corresponding  
199 citations.

## 200 2.3 Data Reduction

### 201 2.3.1 Droplet shattering and cloud contamination

202 Droplet shattering represents a significant source of measurement contamination in airborne aerosol sampling studies.  
203 Weber et al., (1998) described this phenomenon as the fragmentation of cloud droplets during in-cloud measurements,  
204 which can produce artifacts as small as 3 nm that appear in sampling instruments. Similarly, Korolev and Isaac, (2005)  
205 documented comparable shattering effects with ice particles. While a detailed examination of the physical mechanisms  
206 behind droplet shattering lies beyond this study's scope, it is essential to filter such artifacts from our dataset to prevent  
207 misidentification of SPEs.

208 Cloud contamination was systematically detected and eliminated by calculating liquid water content (LWC) using the  
209 approach of Zheng et al., (2021), which utilizes droplet size spectra from the Fast Cloud Droplet Probe (FCDP). Visual  
210 data examination established a detection threshold of  $3 \times 10^{-3} \text{ g m}^{-3}$ , comparable to the  $10^{-3} \text{ g m}^{-3}$  threshold employed  
211 by Zheng et al., (2021). Data exceeding this LWC threshold were excluded from analysis.

### 212 2.3.2 Time lag correction

213 Accurate temporal alignment between the vertical wind speed measured by the AIMMS-20 probe and the particle  
214 concentration measured by the CPCs is essential for reliable flux calculations. Because these instruments were located  
215 at different positions on the aircraft, a time lag exists between the two signals that must be determined and corrected  
216 prior to flux calculation.

217 To confirm that the two CPCs sampled identical air masses simultaneously, Spearman correlation coefficients were  
218 calculated for concentration measurements from both CPCs after removing cloud shattering artifacts and excluding  
219 SPE periods. From the complete campaign dataset, 370 randomly selected seconds of data yielded an average  
220 Spearman correlation coefficient of 0.97 (Supplementary Figs. S1–S2), confirming adequate synchronization between  
221 the two concentration records. However, a high correlation coefficient alone does not determine the precise temporal  
222 offset between the two signals.

**Deleted:** FIMS-derived number concentration also served as a quality control flag for the 3772 CPC, where CPC concentrations less than 10% of corresponding FIMS concentrations were excluded from analysis.

**Deleted:** A single-particle soot photometer (SP2) measured refractory black carbon concentrations in the 50 nm – 500 nm size range. While the SP2 detects individual particles and can provide number concentrations, this study reports mass concentrations ( $\text{ng m}^{-3}$ ) (Schwarz et al., 2006). A high-resolution time-of-flight aerosol mass spectrometer (HR-ToF-AMS) measured bulk nonrefractory aerosol composition including sulfate, nitrate, ammonium, and organics. Dimethylsulfide (DMS) concentrations were measured using a quadruple high-sensitivity Proton-Transfer-Reaction Time-of-Flight Mass Spectrometer (PTR-ToF-MS). Due to measurement uncertainties (Zheng et al., 2021) DMS data indicate presence along the flight track rather than providing precise quantification.

239 Lag times between the two CPC signals were determined individually for every 20-second interval (representing the  
240 time taken for the airplane to traverse 2 km) using covariance maximization, shifting one CPC relative to the other  
241 signal to identify the temporal offset that maximizes their covariance. A single fixed lag time across the entire  
242 campaign was not appropriate, given the variability in lag times observed across flight segments (Supplementary Fig.  
243 S3). This approach was independently validated using pressure measurements from the isokinetic inlet and static  
244 pressure from the AIMMS-20 probe. The two pressure records yielded a Spearman correlation coefficient of 0.99,  
245 confirming that both instruments consistently sampled the same air mass with no systematic offset (Supplementary  
246 Fig. S5). Similarly, covariance maximization applied to the pressure records confirmed that no single lag time was  
247 appropriate across the full campaign (Supplementary Fig. S6), consistent with the CPC-based analysis and further  
248 supporting the use of individually determined lag times for each flux calculation period.

#### 249 2.4 Aerosol number flux calculations

250 Flux measurement methods were originally developed for tower-based platforms, and their application to aircraft  
251 measurements introduces fundamental differences in sampling characteristics that must be carefully considered.  
252 Tower measurements provide continuous observations at fixed heights, capturing the complete turbulent eddy  
253 spectrum including low-frequency contributions essential for accurate flux estimates (Helbig et al., 2021; Sakai et al.,  
254 2001). Aircraft measurements, by contrast, sample different air masses as the platform moves horizontally, effectively  
255 trading temporal for spatial averaging (Desjardins et al., 1989)

256 Three interconnected challenges arise specifically for aircraft-based flux measurements. First, turbulent intensity in  
257 convective boundary layers increases with height above the surface layer before decreasing above  $0.3-0.4 z_i$  (where  $z_i$   
258 is the boundary layer height). Maintaining flux variance within 10% therefore requires measurement lengths of 100  
259 to  $10^4$  times the boundary layer height (Lenschow and Stankov, 1986), a constraint that becomes increasingly difficult  
260 to satisfy at the higher altitudes routinely sampled by research aircraft. Second, high aircraft speeds impose strict  
261 constraints on sensor response times: for an aircraft traveling at  $100 \text{ m s}^{-1}$ , a 1 Hz sampling system resolves eddies no  
262 smaller than 200 m, approaching the lower limit for capturing the dominant flux-carrying scales. The CPCs used in  
263 this study operate at 1 Hz, meaning that contributions from smaller eddies are not resolved and must be accounted for  
264 through flux loss corrections (Section 2.8). Third, and most critically for flux calculation, aircraft measurements are  
265 inherently non-stationary as the platform continuously moves through different air masses, meteorological conditions,  
266 and altitudes. Traditional eddy covariance methods assume stationarity over the averaging period, a condition that is  
267 difficult to maintain during aircraft sampling (Gioli et al., 2004).

268 To address this limitation, this study employs the continuous wavelet transform (CWT) method for flux derivation.  
269 The primary advantage of the CWT approach is that it does not require stationarity and eliminates the need for data  
270 detrending, thereby avoiding systematic errors that can arise from linear detrending procedures (Rannik and Vesala,  
271 1999). This study follows CWT flux derivation method of (Torrence and Compo, 1998), described below.

272 The wavelet coefficient,  $W_N(a,b)$ , for a function  $x(z)$  which changes with height, is calculated as a function of both  
273 location (height for airborne measurements or time for ground-based measurements) and scale (frequency or  
274 wavenumber) through convolution with a wavelet function ( $\psi$ ):

**Deleted:** However, a high correlation coefficient alone does not determine the precise temporal offset between the two signals. C

**Deleted:** ¶

#### 2.3.2 Time lag correction¶

Accurate temporal alignment is critical for flux computations when data originate from multiple instruments in field campaigns. For tower-based or surface measurement systems, temporal synchronization typically employs cross-correlation analysis in which the vertical velocity time series is temporarily shifted (forward or backward) relative to the particle concentration time series (Stull, 1988). Although inlets are usually positioned in close proximity to sample identical air masses, this temporal adjustment is necessary to account for potential transport delays to detectors, which are often located at different positions on the tower. This approach operates on the principle that flux calculations (cross-correlation values) reach their maximum when both signals are optimally synchronized, thereby enabling accurate lag time determination. Similar analysis is essential for aircraft data processing to account for both signal delay (when inlets share the same location, but detectors are positioned differently) and spatial separation effects (when inlets themselves are located at different positions on the aircraft).¶

*Platform-Specific Measurement Characteristics:* Flux measurements differ fundamentally between tower-based and aircraft platforms in their spatial and temporal sampling characteristics. Tower measurements provide continuous observations at fixed heights, capturing the complete turbulent eddy spectrum within the atmospheric boundary layer, including low-frequency contributions essential for accurate flux estimates (Helbig et al., 2021; Sakai et al., 2001). Aircraft measurements sample different air masses as the platform moves horizontally, effectively trading temporal for spatial averaging (Desjardins et al., 1989). Aircraft measurements at higher boundary layer altitudes face additional challenges. In convective boundary layers, turbulent intensity increases with height above the surface layer before decreasing after  $0.3-0.4 z_i$  (where  $z_i$  is the boundary layer height), requiring measurement lengths of 100 to  $10^4$  times the boundary layer height to maintain flux variance within 10% (Lenschow and Stankov, 1986). For aircraft traveling at  $100 \text{ m s}^{-1}$ , a 10 Hz sampling system resolves eddies as small as 20 m, while a 1 Hz sampling system resolves eddies down to 200 m.¶

Tower measurements easily satisfy stationarity requirements through 30-minute averaging periods, whereas aircraft measure turbulence over large areas much faster but must assume spatial homogeneity along the flight path (Gioli et al., 2004). High aircraft speeds introduce additional constraints on sensor response times and spatial resolution, as instruments must respond quickly enough to resolve the smallest relevant eddies, a challenge that intensifies at higher flight speeds and lower altitudes where smaller eddy sizes result in higher observed frequencies when sampled by fast-moving aircraft (Desjardins et al., 1989)¶

*CPC synchronization validation:* Since the CPCs used in this study were connected to the same isokinetic inlet from different positions, confirmation was needed that they sampled identical air masses simultaneously. Supplementary Figure S1 shows particle concentration measurements from both CPCs for a representa... [1]

**Deleted:** ¶

**Deleted:** over traditional methods

**Deleted:** conditions

**Deleted:** preventing

**Deleted:** in flux calculations

**Deleted:** the method

**Deleted:** of

**Deleted:** for CWT flux derivation

424 
$$W_N(a, b) = \int_{-\infty}^{\infty} x(z) \psi_{a,b}(z) dz \quad (1)$$

Deleted:

425 where  $(z)$  represents the wavelet function, controlled by the scale parameter  $(a)$  and translation parameter  $(b)$ . The  
 426 scale parameter governs the wavelet frequency, while the translation parameter shifts it in the temporal domain. The  
 427 wavelet function is defined as:

428 
$$\psi_{a,b}(z) = \frac{1}{\sqrt{a}} \psi_0\left(\frac{z-b}{a}\right) \quad (2)$$

Deleted:

429 All wavelet functions are based on a “mother” wavelet. For this study, the Morlet wavelet is chosen as the mother  
 430 wavelet, which is the product of a plane wave with a Gaussian function (Torrence and Compo, 1998). Schaller et al.,  
 431 (2017) reported that the Morlet wavelet provides reliable results in flux analysis even when traditional eddy covariance  
 432 methods fail.

433 
$$\psi_0(\eta) = \pi^{-\frac{1}{4}} e^{i\omega_0\eta} e^{-\frac{\eta^2}{2}} \quad (3)$$

Deleted:

434 where  $\omega_0$  is the non-dimensional frequency (set to 6 for this study), and  $\eta$  is the non-dimensional time parameter and  
 435 , the first exponential term is the complex sinusoid, and the second exponential term is the Gaussian envelope. Using  
 436 this methodology, the vertical turbulent particle flux can be calculated according to (Schaller et al., 2017; Torrence  
 437 and Compo, 1998) as:

Deleted: -

Deleted: -

438 
$$\overline{w'(z)N'_{s-10}(z)} = \frac{\delta t}{c_s} \times \frac{\delta_j}{L} \times \sum_{n=0}^{L-1} \sum_{j=0}^J \left[ \frac{W_N(a,b) \times W_w^*(a,b)}{a(j)} \right] \quad (4)$$

Deleted:

439  $C_6$ , the wavelet specific reconstruction factor is taken as 0.776, which is empirically derived for the chosen wavelet  
 440 (Schaller et al., 2017; Torrence and Compo, 1998) ,  $L$  represents the number of elements in the time series with  
 441 timestep  $\delta_t$ , which is the inverse of frequency (1 Hz for this study),  $J$  is the maximum number of scales with  $\delta_j$  being  
 442 the space between each discrete scale (Schaller et al., 2017; Torrence and Compo, 1998).

443 
$$J = \delta_j^{-1} \times \log_2\left(\frac{L \times \delta_t}{s_0}\right) \quad (5)$$

444  $\delta_j$  was chosen to be 0.25 s (Schaller et al., 2017; Torrence and Compo, 1998), this value can be adjusted to get better  
 445 scale resolution at the expense of higher computational cost,  $s_0$  is the smallest scale of the wavelet taken as  $2\delta_t$ ,  $a(j)$  is  
 446 the scale parameter for the discrete scale calculated as:

447 
$$a(j) = s_0 \times 2^{j\delta_j} \quad j = 0, 1, \dots, J \quad (6)$$

Deleted:

448  $W_N(a,b)$  is the wavelet coefficient for the particle concentration signal, and  $W_w^*(a,b)$  is the complex conjugate of the  
 449 wavelet coefficient for the vertical velocity signal. Under stationary conditions, fluxes calculated using both CWT and

457 traditional eddy covariance methods should yield equivalent results, though agreement may vary in aircraft  
458 measurements due to the presence of non-stationarities (Misztal et al., 2014; Wolfe et al., 2018).

## 459 2.5 Limit of Detection Determination

460 Spirig et al., (2005) demonstrated that calculating covariance at time ranges significantly larger than the integral time  
461 scale can quantify the precision of individual flux determinations. The integral time scale was calculated using the  
462 cross-correlation function between vertical wind  $w$  and 3-10 nm sized particle size concentration, using the method  
463 described by (Lenschow et al., 2000; Wulfmeyer et al., 2016). The cross covariance is given as:

$$464 A_{xy}(\tau) = \text{cov}(x_t, y_{t+\tau}) \quad (7)$$

465 Where  $x_t$  and  $y_t$  are the two signals of interest, with  $y$  shifted by the lag time  $\tau$ . Now the cross covariance is fitted to a  
466 model of the form:

$$467 A_{\text{model}}(\tau) = v - k\tau^2 \quad (8)$$

468 Where  $v$  and  $k$  are fitted parameters. The line is fitted till the first zero crossing of the cross covariance. And using  
469 this, the integral timescale,  $I$  is calculated as:

$$470 I = \frac{2}{5} \left( \frac{v}{k} \right)^{3/2} \quad (9)$$

471 The median value of the integral timescale for the flux events was  $\sim 11$  seconds. The limit of detection (LoD) is  
472 defined as 1.96 times (95% confidence interval) the standard deviation of covariance between  $w$  and  $N_{3-10}$  when one  
473 of the signals is temporarily shifted with respect to the other. To estimate the precision of an individual flux  
474 determination, we followed Spirig et al. (2005) and examined fluctuation of the covariance function at time lags far  
475 away from the true lag. The standard deviations of the covariance function were calculated between 4500 to 5700  
476 seconds (corresponding to 45 to 57 km spatial displacement) before and after the peak fluxes. These lag times were  
477 selected to be much higher than the integral timescale of turbulence at all measurement heights. The limit of detection  
478 (LoD) is defined as 1.96 times (95% confidence interval) the standard deviation of covariance between  $w$  and  $N_{3-10}$   
479 when one of the signals is temporarily shifted with respect to the other. Signal shifts  $-10$  to  $+10$  seconds  
480 (corresponding to  $\pm 1$  km spatial displacement) are applied to ensure complete decoupling between the signals. Flux  
481 calculations are restricted to periods when the aircraft maintained horizontal, straight line flight segments to ensure  
482 reliable flux estimates and minimize the influence of aircraft maneuvers on turbulence measurements. The limit of  
483 detection is used as an absolute value and hence if a particular flux event is lower in absolute value compared to the  
484 LoD, they will not be considered for analysis.

## 485 2.6 Small particle events selection criteria

486 Establishing appropriate threshold values for new particle formation over tropical oceanic regions presents significant  
487 challenges due to sparse observational datasets and the intricate interactions between meteorological and chemical  
488 processes in these environments. Earlier studies have typically used concentration thresholds of  $10^3$  to  $10^4$  particles  
489  $\text{cm}^{-3}$  for ultrafine particles (3–25 nm) to distinguish nucleation events from background conditions. However, these

Formatted: Font color: Blue

Formatted: Font color: Blue

Formatted: Font color: Blue

Formatted: Font color: Blue

Formatted: Font color: Blue

Formatted: Font color: Blue

Formatted: Font color: Blue

Formatted: Font color: Blue, Subscript

Formatted: Font color: Blue, Subscript

Formatted: Font color: Blue

Deleted: (

Deleted: ,

Formatted: Font color: Blue

Deleted: Since the integral time scale cannot be accurately determined in this study, we employ a large time range approach

Formatted: Line spacing: 1.5 lines

494 criteria were primarily established based on observations from continental or mid-latitude marine environments (Dal  
495 Maso et al., 2005; Kulmala et al., 2012). Given that tropical marine regions are characterized by reduced background  
496 aerosol loadings and distinct precursor gas profiles relative to higher latitude zones, more conservative thresholds  
497 (500–1000 particles  $\text{cm}^{-3}$ ) may prove better suited for detecting nucleation phenomena in these relatively unpolluted  
498 environments (Modini et al., 2009; Weber et al., 1997). Additionally, the aircraft-based measurement method  
499 prevented the implementation of traditional nucleation event identification criteria, specifically the requirement for  
500 persistent concentration increases spanning 1–2 hours to distinguish genuine nucleation from brief local source  
501 influences (Kulmala et al., 2012).

Deleted: (Dal Maso et al., 2005; Kulmala et al., 2012)

502 For this study, we modified the methodology established by Zheng et al., (2021) to detect small particle  
503 events (SPEs). Individual 1-second measurements were used to identify when  $N_{3-10}$  concentrations exceeded  $150 \text{ cm}^{-3}$ ,  
504 once identified the measurements that exceeded the threshold were grouped into 10-second intervals (equivalent to ~1  
505 km spatial resolution), and the average  $N_{3-10}$  for the group was checked to see if it achieved statistical significance  
506 using:

$$507 \quad N_3 - N_{10} > 3\sigma_D$$

(10)

Deleted: 7

508 where  $\sigma_D$  represents the uncertainty in the concentration difference between  $N_3$  and  $N_{10}$ , expressed as:

$$509 \quad \sigma_D = \sigma(N_3 - N_{10})$$

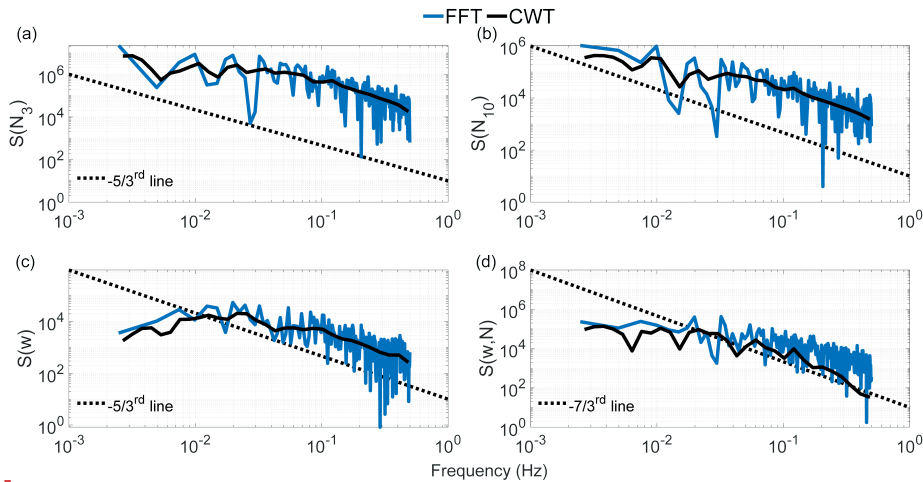
(11)

Deleted: 8

Formatted: Line spacing: 1.5 lines

## 510 2.7 Frequency response and flux averaging time

511 Momentum, enthalpy, and matter are transported in the atmosphere by eddies of different spatial scales. One-  
512 dimensional power spectral analysis is used to decompose the signal into components of different frequencies, which  
513 are associated with different eddy sizes. Fast Fourier Transform (FFT) and Continuous Wavelet Transform (CWT)  
514 were used to calculate the power spectral density (PSD) of vertical wind speed and particle concentration.



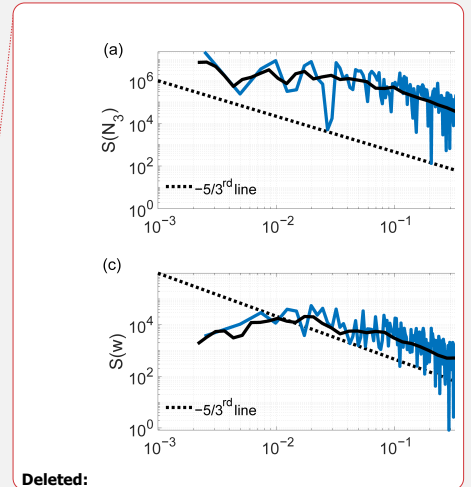
518

519 **Figure 1. Power spectral density for (a)  $N_3$ , (b)  $N_{10}$ , (c) vertical wind velocity, and (d) 3-10 nm particle flux.**

520 Figure 1 shows the PSD for a flight leg on 21 June 2017 between 13:43 and 13:49 UTC at a height of 550 m above  
 521 mean sea level. Dashed lines represent the theoretical slopes for the inertial subrange, which describe how energy  
 522 cascades from larger to smaller eddies and finally dissipates as heat due to viscous friction (Pope, 2000). **Both particle**  
 523 **concentration spectra (Figs. 1a,b) and the flux spectrum (Fig. 1d) broadly follow the theoretical  $-5/3$  and  $-7/3$**   
 524 **Kolmogorov scaling across the resolved frequency range. The supplementary figure comparing 1 Hz and 10 Hz**  
 525 **vertical wind velocity spectra (Supplementary Fig. S7) confirms that turbulent energy exists at scales beyond the 1 Hz**  
 526 **Nyquist frequency. The absence of a visible noise floor in the particle concentration spectra at high frequencies reflects**  
 527 **the band-limited response of the CPC, which acts as a low-pass filter that attenuates high-frequency concentration**  
 528 **fluctuations, producing a steep spectral roll-off rather than a white noise floor. While this results in a cleaner spectrum**  
 529 **visually, it still represents real flux loss at high frequencies that is accounted for through the correction described in**  
 530 **Section 2.8.**

531

532 Figure 1 also shows some differences between FFT and CWT flux calculations, especially for fluxes at high  
 533 frequencies. These differences are attributable primarily to non-stationarity in the aircraft data, as the platform moves  
 534 through different air masses, meteorological conditions, and altitudes. FFT assumes stationarity over the entire  
 535 analysis window and can therefore introduce artifacts under such conditions, whereas CWT provides time-localized  
 536 frequency information that is more robust for non-stationary signals (Schaller et al., 2017). Li et al., (2023) evaluated  
 537 uncertainties of turbulent flux calculation using both methods, finding that biases can range from 50–100% of the  
 538 spectrally complete flux. We note that the high-frequency deviations visible in the particle concentration spectra are  
 539 not a consequence of FFT limitations but reflect the band-limited response of the CPC, which attenuates concentration



Deleted:

Formatted: Space After: 12 pt

Deleted:

Deleted: Both particle concentration spectra (e.g., Fig. 1b) and flux spectra (Fig. 1d) exhibit deviations from the theoretical  $-5/3$  and  $-7/3$  Kolmogorov scaling at frequencies larger than 0.3 Hz. The spectral flattening observed at these frequencies is characteristic of white noise, suggesting instrumental limitations where the CPC cannot adequately resolve concentration fluctuations faster than  $\sim 3$  sec.

Deleted: likely stem from several key methodological differences. Aircraft data are inherently non-stationary as the platform moves through different air masses, meteorological conditions, and altitudes. FFT assumes stationarity over the entire analysis window, which can introduce artifacts at high frequencies when applied to non-stationary aircraft data. CWT can handle non-stationary signals by providing time-localized frequency information, making it more robust for aircraft measurements (Schaller et al., 2017).

Deleted: eddy covariance and wavelet analysis

Deleted: "EC and Morlet-wavelet generate

Deleted: ranging

Deleted: 'true'

Deleted: values

Deleted: FFT can suffer from spectral leakage, especially at high frequencies, when the raw signal doesn't fit perfectly into the sine or cosine signal in the analysis window. This is particularly problematic for aircraft data, where turbulent structures may not be periodic over the sampling interval (Harris, 1978). CWT uses wavelets that are naturally windowed and localized, reducing leakage effects. ...

Formatted: Font color: Blue

569 fluctuations at frequencies above ~0.3 Hz, as discussed in Section 2.8. The CWT's more conservative high-frequency  
570 response may better represent the actual resolvable flux contributions (Misztal et al., 2014).

571 To assess whether the calculated fluxes adequately represent both low- and high-frequency turbulent contributions,  
572 we conducted ogive analysis using the approach described by Foken et al., (2006). Mobile measurement platforms  
573 necessitate modified considerations for flux averaging intervals. Standard 30-minute averaging periods used in  
574 stationary tower observations are inappropriate for aircraft measurements. Considering the aircraft's ground speed, a  
575 90-second sampling period covers an equivalent air mass to that sampled by a stationary sensor over 30 minutes at  
576 typical wind speeds of  $5 \text{ m s}^{-1}$ . To enable direct comparison between ogives computed using FFT and CWT methods,  
577 normalization was applied according to Sun et al., (2018):

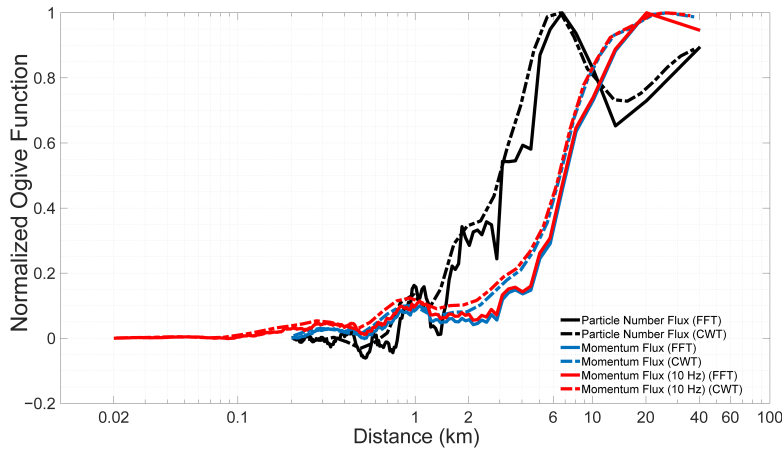
$$578 \quad \sigma_g(f) = \frac{og(f)}{sgn(\max(og(f)) + \min(og(f))) \max(|og(k)|)} \quad (12)$$

579 where  $sgn\{x\}$  represents the signum function, returning +1 for positive  $x$ , -1 for negative  $x$ , and zero when  $x$  equals  
580 zero. When the normalized ogive equals 1, the ogive value corresponds precisely to the covariance value for that  
581 averaging period. The advantage of this normalization approach is that it facilitates the identification of cases where  
582 low-frequency turbulence has an opposite sign to high-frequency turbulence. In such situations, large and small eddies  
583 transport material in opposing directions, indicating complex atmospheric processes such as counter-gradient  
584 transport. The normalized ogive plot visually reveals these opposing contributions through characteristic rise-and-fall  
585 patterns that might otherwise be obscured in non-normalized data.

586 Figure 2 illustrates the ogive as a function of distance covered by the aircraft for the same flight leg shown in Fig. 1.  
587 Signal frequency was converted to distance by dividing the aircraft speed (assumed to be constant at  $100 \text{ m s}^{-1}$ ) by the  
588 frequency obtained from the FFT or CWT analysis. This plot reveals that the particle flux for this flight leg can be  
589 resolved by averaging over 40 km. While both FFT and CWT ogives show agreement for this case, such consistency  
590 cannot be expected universally; therefore, CWT fluxes are used throughout this study for the reasons discussed in  
591 previous sections.

**Deleted:** At high frequencies corresponding to small spatial scales, aircraft measurements become increasingly challenging due to sensor response time limitations, spatial averaging effects, and platform motion artifacts (more on this in Sect. 2.8).

**Deleted:** 9



597

598 **Figure 2:** Normalized ogive function as a function of distance covered by the aircraft. The ogive represents the cumulative  
 599 fractional contribution to total flux from high to low frequencies.

Deleted: Normalized ogive function.

600 **2.8 Flux loss correction**

601 If the sensor used to measure fluxes are too slow to accurately capture the smaller eddies that contribute to the total  
 602 flux, the turbulent fluxes will require correction. For micrometeorological flux measurements on towers at 10 m above  
 603 the surface, instruments are typically operated at 10 Hz (Nyquist frequency = 5 Hz). Under typical wind speeds of 5  
 604 m s<sup>-1</sup>, this sampling rate can resolve eddies as small as ~1 m, ensuring that most energy-containing and inertial  
 605 subrange eddies are captured (Aubinet et al., 2012; Lee et al., 2005; Stull, 1988).

606 However, airborne flux measurements present different challenges. The integral length scales of turbulent eddies  
 607 increase approximately linearly with height within the surface layer (roughly the bottom 10% of the boundary layer),  
 608 then remain approximately constant above this level, limited by the boundary layer height (Kaimal and Finnigan,  
 609 1994). In the mixed layer portion of a typical boundary layer (above ~100 m surface layer), integral length scales are  
 610 typically 100-200 m (Lenschow and Stankov, 1986). At an aircraft ground speed of 100 m s<sup>-1</sup>, the 1 Hz sampling  
 611 provides 200 m spatial resolution, which approaches but does not fully resolve the integral length scale. Consequently,  
 612 the sampling resolution approaches the lower limit for adequately resolving the dominant flux-carrying scales and  
 613 may under sample contributions from smaller turbulent structures.

614 To address this limitation, we applied the approximations from Horst (1997) to estimate the ratio of measured flux  
 615 ( $F_m$ ) to spectrally complete flux ( $F$ ) for different atmospheric stability conditions encountered during campaign flights:

616 
$$\frac{F_m}{F} = \frac{1}{1 + (2\pi n_m \tau_c \frac{u}{z})^\alpha} \quad (13)$$

617 where  $F_m$  is the measured flux,  $F$  is the spectrally complete flux,  $u$  is the magnitude of average wind speed,  $z$  is the  
 618 height of the airplane,  $\tau_c$  is the response time constant of the CPC, which was taken as 3.0 s,  $\alpha =$  seven-eights- and  $n_m$

Deleted: "true"

Deleted:

Deleted: 0

Deleted: "true"

624 = 0.085 for neutral and unstable conditions (Pryor et al., 2007). Equation 13 was originally developed by Horst (1997)  
625 to estimate the attenuation of scalar flux measurements within the surface layer, but has been applied to aircraft  
626 measurements (Gioli et al., 2004), with corrected airborne fluxes showing good agreement with tower data when  
627 aircraft measurements were conducted over homogeneous surfaces at altitudes comparable to tower height.

628 To illustrate the practical importance of this correction, the  $\frac{F_m}{F}$  ratio varies substantially depending on measurement  
629 height and atmospheric stability conditions encountered during the campaign. For measurements conducted near the  
630 top of the marine boundary layer (~1,200–1,400 m) under near-neutral to unstable conditions,  $\frac{F_m}{F}$  values approach  
631 unity (0.93–0.99), indicating that flux losses are modest at these heights where the dominant flux-carrying eddies are  
632 large relative to the CPC response limitation. However, for measurements conducted closer to the surface (~30–550  
633 m),  $\frac{F_m}{F}$  values range from 0.70 to 0.95, implying that uncorrected fluxes could underestimate the spectrally complete  
634 flux by up to 30%. This highlights the importance of applying the flux loss correction, particularly for low-altitude  
635 flight legs where eddy sizes are smaller and the CPC response time constant becomes a more significant fraction of  
636 the dominant flux-carrying eddy turnover times.

637 Following the approach of (Islam et al., 2022), we assessed the random uncertainty in particle flux due to counting  
638 statistics. We found it to be 2–3 orders of magnitude lower compared to the measured flux magnitudes reported in this  
639 study. Therefore, the correction due to discrete counting statistics of CPCs was not applied to this study.

### 640 3.0 Results

641 We examine two flight days as case studies of SPEs observed at varying altitudes above the ocean. Additional  
642 supporting flights are presented in the Supplementary Information. Table 1 summarizes the  $N_{3-10}$  vertical turbulent  
643 flux estimates derived from all six flight days analyzed in this study, grouped by the inferred nucleation regime. Flights  
644 1 and 2 (January 29 and February 10, 2018) are classified as entrainment zone nucleation events, where SPEs were  
645 detected near the top of the MBL at heights exceeding 1,200 m. Flights 3–6 (June 21 and July 7, 2017; February 18  
646 and 12, 2018) are classified as decoupled layer nucleation events, with SPEs observed across a broader range of  
647 altitudes (30–837 m). For all events, the ratio of measured flux to the spectrally complete flux  $\left(\frac{F_m}{F}\right)$  exceeds 0.76,  
648 indicating minimal flux loss due to sensor response limitations. The normalized vertical velocity variance  $(\sigma_w^2 w_*^{-2})$   
649 is generally low, consistent with relatively quiescent turbulent conditions during the measurement periods. Negative  
650 flux values indicate downward transport of freshly nucleated particles from the entrainment zone toward the surface,  
651 while positive values suggest upward transport from a source within the decoupled sub-cloud layer. Two of these  
652 flight days, January 29, 2018 (Case 1) and June 21, 2017 (Case 2), are examined in detail as case studies in the  
653 following sections, with the remaining four flights presented as supporting examples in the Supplementary  
654 Information.

655 Table 1. Summary of  $N_{3-10}$  particle vertical turbulent flux estimates from aircraft campaigns with detection limits and  
656 flux loss assessment.

Deleted: 10

Formatted: Font color: Blue

Deleted: We examine two flight days as case studies of SPEs observed at varying altitudes above the ocean. Additional supporting flights are presented in the Supplementary Information for each case

Deleted: [Table 1. Summary of  \$N\_{3-10}\$  particle vertical turbulent flux estimates from aircraft campaigns with detection limits and flux loss assessment. ...](#)

<u>No</u>	<u>Date</u>	<u>Time (UTC)</u>	<u>Height (m)</u>	<u>N<sub>3-10</sub> flux (cm<sup>-2</sup> s<sup>-1</sup>)</u>	<u>LoD (cm<sup>-2</sup> s<sup>-1</sup>)</u>	<u>F<sub>m</sub>/F</u>	<u>σ<sup>2</sup> w<sub>c</sub><sup>-2</sup></u>
<b><u>Entrainment zone nucleation</u></b>							
<u>1</u>	<u>01/29/18</u>	<u>10:54:59-10:58:13</u>	<u>1,205</u>	<u>-41,092</u>	<u>34,423</u>	<u>0.97</u>	<u>0.01</u>
		<u>12:18:47-12:21:50</u>	<u>1,218</u>	<u>-2,975</u>	<u>2,085</u>	<u>0.98</u>	<u>0.005</u>
<u>2</u>	<u>02/10/18</u>	<u>13:53:20-13:55:02</u>	<u>1,375</u>	<u>-1,195</u>	<u>381</u>	<u>0.93</u>	<u>0.003</u>
<b><u>Decoupled layer nucleation</u></b>							
<u>3</u>	<u>06/21/17</u>	<u>14:03:30-14:09:25</u>	<u>800</u>	<u>1,139</u>	<u>294</u>	<u>0.99</u>	<u>0.016</u>
		<u>13:56:10-14:02:25</u>	<u>800</u>	<u>2,929</u>	<u>1,239</u>	<u>0.98</u>	<u>0.021</u>
		<u>13:42:40-13:49:23</u>	<u>550</u>	<u>-2,782</u>	<u>1,995</u>	<u>0.95</u>	<u>0.1</u>
		<u>13:32:20-13:38:40</u>	<u>30</u>	<u>-860</u>	<u>400</u>	<u>0.76</u>	<u>0.17</u>
<u>4</u>	<u>07/07/17</u>	<u>13:42:18-13:43:04</u>	<u>565</u>	<u>-94,093</u>	<u>49,410</u>	<u>0.86</u>	<u>0.02</u>

		<a href="#">13:43:07-13:44:58</a>	<a href="#">535</a>	<a href="#">-21,317</a>	<a href="#">4,959</a>	<a href="#">0.90</a>	<a href="#">0.031</a>
<a href="#">5</a>	<a href="#">02/18/18</a>	<a href="#">14:17:32-14:19:38</a>	<a href="#">555</a>	<a href="#">298</a>	<a href="#">115</a>	<a href="#">0.81</a>	<a href="#">0.016</a>
		<a href="#">14:47:10-14:51:34</a>	<a href="#">250</a>	<a href="#">-3,217</a>	<a href="#">1,153</a>	<a href="#">0.70</a>	<a href="#">0.056</a>
<a href="#">6</a>	<a href="#">02/12/18</a>	<a href="#">14:54:27-14:58:37</a>	<a href="#">837</a>	<a href="#">5,433</a>	<a href="#">1,173</a>	<a href="#">0.93</a>	<a href="#">0.04</a>

665 **Case 1: SPE occurring in the entrainment zone near the top of the marine boundary layer**

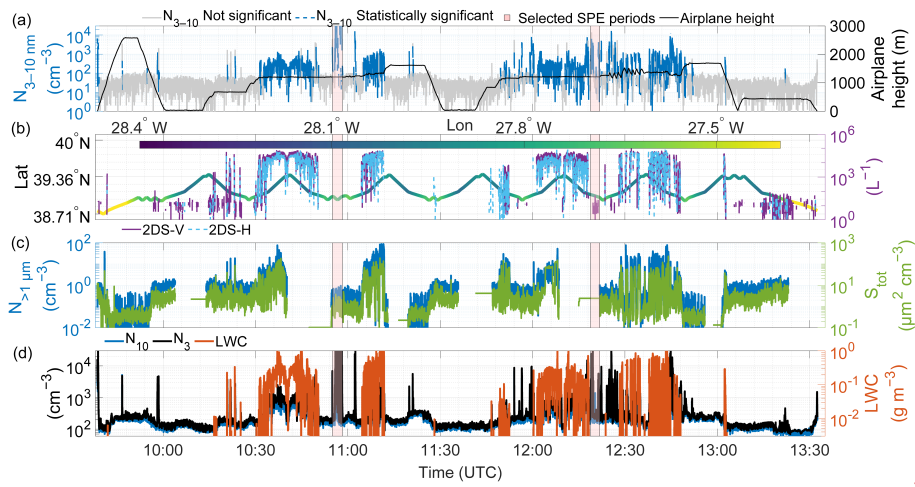
666 [Figures 3–5](#) present data collected on January 29, 2018 with an additional example from February 10, 2018, shown in  
667 [Supplementary Figs. S8–S10](#). Back-trajectory analysis (not shown) indicates that the sampled airmasses had been  
668 circulating around the Azores for the preceding three days and were therefore likely less polluted than North American  
669 outflow air masses. Figure 3 shows a multi-panel time series covering approximately 3.5 hours of flight operations.  
670 The aircraft initially ascended to ~2,500 m but generally remained below ~1,500 m for most of the flight (Fig. 3a).  
671 The flight trajectory (Fig. 3b) reflects predominantly east-west movement across the Azores region, spanning latitudes  
672 from approximately 38.7° to 39.4°N and longitudes from -28.4° to -27.4°W. Drizzle number concentration measured  
673 by 2DS (purple and blue lines in Fig. 3b) was absent or low during the selected SPE periods. Elevated drizzle number  
674 concentration, together with high liquid water content regions (orange in Fig. 3d), mark frequent cloud encounters.  
675 Following our quality control procedures, all  $N_{3-10}$  concentration data with  $LWC \geq 3 \times 10^{-3} \text{ g m}^{-3}$  were excluded from  
676 analysis to avoid contamination from cloud droplet shattering artifacts. Pink-shaded periods mark the intervals chosen  
677 for detailed analysis, which exhibited simultaneous increases in both  $N_3$  and  $N_{10}$  concentrations exceeding  $10^4 \text{ cm}^{-3}$   
678 (indicating an SPE). Supermicron particle concentration (blue in Fig. 3c) as well as total particle surface area (green  
679 in Fig. 3c) were also low during the selected SPE periods, indicating the absence of particles such as sea spray aerosols.  
680

Formatted: Font color: Blue

Deleted: 7

Deleted: 9

Formatted: Font color: Blue



683

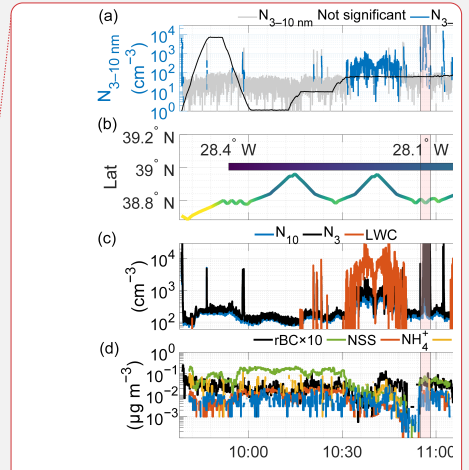
684

685

686

687

Figure 3. Multi-parameter time series from the January 29, 2018 flight, (a)  $N_{3-10}$  particle concentrations and aircraft altitude; (b) aircraft position (latitude and longitude) and drizzle number concentration; (c) supermicron particle concentration and total particle surface area ( $S_{\text{tot}}$ ); (d) particle number concentrations ( $N_{10}$  and  $N_3$ ) and liquid water content. Gaps in the time series indicate the missing data.



Deleted:

Formatted: Font: 9 pt, Font color: Blue

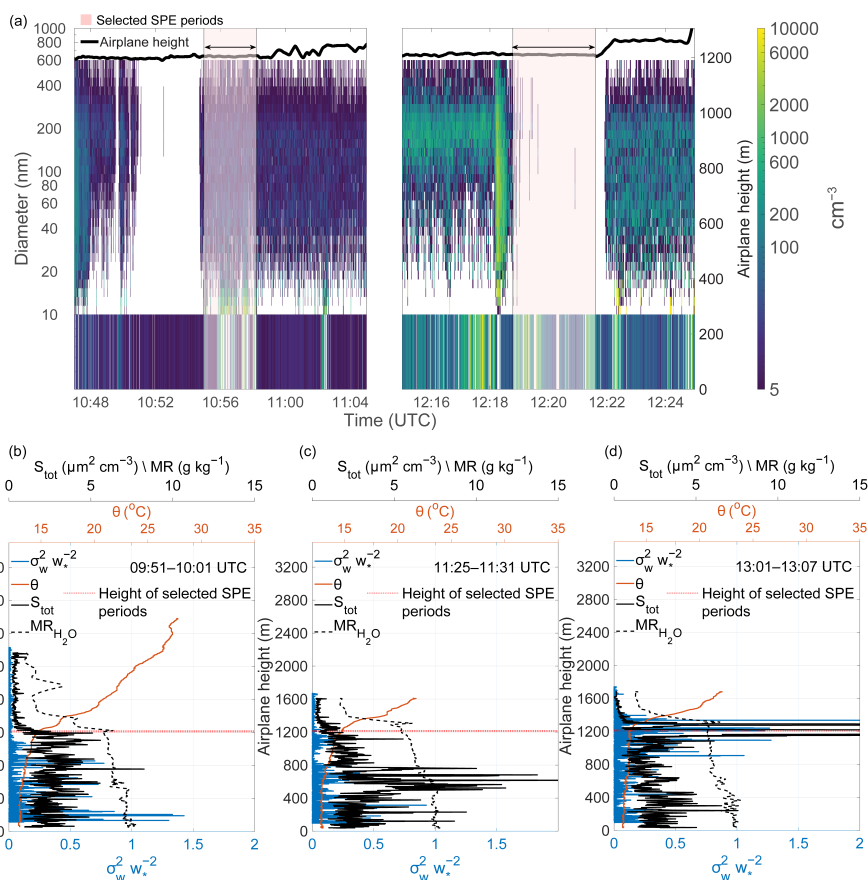
Formatted: Font: 9 pt

Formatted: Font: 9 pt

Formatted: Font: 9 pt

Formatted: Font: 9 pt, Font color: Blue, English (US)

Formatted: Font: 9 pt, Font color: Blue



689

690 **Figure 4. (a) Size-resolved particle number concentrations (10–600 nm) from FIMS as a function of time and altitude, with**  
 691  **$N_{3-10}$  concentrations shown in the lower strip. Pink shading indicates selected SPE periods. (b-d) Vertical profiles of**  
 692 **potential temperature ( $\theta$ ), normalized vertical velocity variance ( $\sigma_w^2 w_*^{-2}$ ), total particle surface area ( $S_{\text{tot}}$ ), and water vapor**  
 693 **mixing ratio (MR<sub>H<sub>2</sub>O</sub>) for three time periods nearest to the selected SPE periods: (b) 09:51–10:01 UTC, (c) 11:25–11:31**  
 694 **UTC, and (d) 13:01–13:07 UTC. Gaps in the time series indicate the missing data.**

695

696 Figure 4a shows the temporal evolution of particle concentration between ~10:47–11:05 and ~12:15–12:25 UTC. The  
 697 colormap represents FIMS-derived, size-resolved aerosol number concentrations (10–600 nm diameter), varying  
 698 across time and altitude, while the lower panel displays  $N_{3-10}$  concentrations. The two pink-highlighted intervals are  
 699 the same as in Fig. 3. The high particle concentration spike observed ~12:18 UTC coincides with elevated LWC and  
 700 drizzle concentration (Fig. 3d) and was excluded from analysis following our quality control procedures (Section  
 701 2.3.1). Weber et al., (1998) documented that cloud droplet shattering can produce artifactual particle concentrations as

**Deleted:** Figure 3. Multi-parameter time series during the January 29, 2018 flight showing: (a)  $N_{3-10}$  particle concentrations with aircraft altitude (b) aircraft position with latitude and longitude; (c) particle number concentrations for  $N_{10}$ ,  $N_{3}$ , and liquid water content; and (d) non-refractory aerosol chemical composition including non-seasalt sulfate (NSS), ammonium ( $\text{NH}_4^+$ ), organics (Org), chlorine ion ( $\text{Cl}^-$ ), refractory black carbon (rBC, multiplied by 10 for visualization) in  $\mu\text{g m}^{-3}$ , and trace gases dimethylsulfide (DMS) and methanol in ppbv. Figure 3 presents a multi-panel time series spanning approximately 3.5 hours of flight operations. The aircraft first ascended to ~2,500 m but generally operated below ~1,500 m throughout the flight (Fig. 3a). The flight trajectory (Fig. 3b) demonstrates predominantly east-west movement across the Azores region, spanning latitudes from approximately  $39.0^{\circ}$  to  $39.5^{\circ}\text{N}$  and longitudes from  $-28.4^{\circ}$  to  $-27.4^{\circ}\text{W}$ . High liquid water content regions (orange in Fig. 3c) indicate frequent cloud encounters. Following our quality control procedures, all  $N_{3-10}$  concentration data with liquid water presence were excluded from analysis to prevent contamination from cloud droplet shattering artifacts. The pink-shaded periods mark the intervals chosen for detailed analysis, which exhibited simultaneous increases in both  $N_3$  and  $N_{10}$  concentrations exceeding  $10^6 \text{ cm}^{-3}$  (indicating an SPE). Figure 3d demonstrates that these periods contained no measurable liquid water and were distinguished by substantial concentrations ( $\sim 0.1 \mu\text{g m}^{-3}$ ) of non-seasalt sulfate. Organic concentrations were also elevated throughout the flight, especially during the second half.

**Deleted:** Figure 4. (a) The main panel shows size-resolved particle number concentrations (10-600 nm) from FIMS as a function of time and altitude, while  $N_{3-10}$  concentrations in the lower strip. (b-d) Vertical profiles of potential temperature ( $\theta$ ), normalized vertical velocity variance ( $\sigma_w^2 w_*^{-2}$ ), particle total surface area ( $S_{\text{tot}}$ ), and water vapor mixing ratio (MR). Gaps in the time series indicate the missing data.

**Deleted:** (

**Deleted:** ,

738 small as 3 nm in airborne CPC measurements, making this the most plausible explanation for the observed spike.  
 739 Aircraft exhaust contamination can be ruled out, as the nearest prior flight transect over this region occurred  
 740 approximately half an hour earlier at an altitude ~60 m lower, more than sufficient time and vertical separation for  
 741 complete plume dispersal. This data point was therefore excluded from all flux calculations as the concurrent LWC  
 742 exceeded the quality control threshold of  $3 \times 10^{-3} \text{ g m}^{-3}$ .  
 743 Figures 4b–d present vertical profiles of potential temperature, normalized vertical velocity variance ( $\sigma_w^2 w_*^{-2}$ ) i.e.,  
 744 (the vertical velocity variance normalized by the square of the convective velocity scale), total particle surface area,  
 745 and the water vapor mixing ratio at three locations nearest to the pink-highlighted intervals. Sharp gradients in the  
 746 potential temperature (orange) mark the top of the MBL, defining the capping inversion that suppresses vertical mixing  
 747 between the boundary layer and the free troposphere. The co-occurrence of these temperature gradients with elevated  
 748 normalized vertical velocity variance ( $\sigma_w^2 w_*^{-2}$ ) near the inversion level indicates the presence of an entrainment zone,  
 749 where thermodynamic forcing (including cloud-top radiative cooling and wind shear) drives mixing between the free  
 750 tropospheric air above and the convective boundary layer below (Boers and Eloranta, 1986). Figures 4b–d reveal a  
 751 deep boundary layer with the entrainment zone between approximately 1,200–1,400 m, consistent with previous  
 752 estimates that entrainment zones typically comprise 20–40% of boundary layer depth (Martin et al., 2014).  
 753 Figures 4b–d present the profiles of ( $\sigma_w^2 w_*^{-2}$ ) profiles, a metric that characterizes the intensity of turbulent structures  
 754 in convective boundary layers (Deardorff, 1974; Dewani et al., 2023). These profiles show elevated ( $\sigma_w^2 w_*^{-2}$ ) values  
 755 near the ocean surface and within the entrainment zone, with minimal values in the free troposphere, where significant  
 756 turbulence is absent.  
 757 The water vapor mixing ratio profiles in Figs. 4b–d reveal evolving boundary layer moisture structure during the  
 758 flight. The early profile (Fig. 4b) shows a relatively well-mixed moisture distribution below the capping inversion at  
 759 ~1,200 m, with a sharp decrease into the drier free troposphere above. The latter profiles (Figs. 4c–d) exhibit a two-  
 760 step moisture structure, with a sharper gradient near ~600 m suggesting progressive decoupling of the boundary layer  
 761 during the course of the flight, separating a moister surface layer from a drier sub-cloud layer above. Despite some  
 762 vertical variability shown in Figs. 4b–d, the total particle surface area ( $S_{\text{tot}}$ ) remained relatively low throughout the  
 763 flight, falling well below the campaign averages of  $\sim 30 \text{ } \mu\text{m}^2 \text{ cm}^{-3}$  in the surface mixed layer and  $\sim 10 \text{ } \mu\text{m}^2 \text{ cm}^{-3}$  in the  
 764 upper decoupled layer reported by Zheng et al. (2021). Figure 4c also shows a distinct  $S_{\text{tot}}$  maximum at an altitude  
 765 where small gradients in both potential temperature and mixing ratio suggest the presence of an entrainment layer.  
 766 The pronounced  $S_{\text{tot}}$  increase could indicate a nucleation occurring at this location (see Case 2 below), although this  
 767 hypothesis could not be independently verified looking at the  $N_{3-10}$  data in this case. Figure 4c shows that the  
 768 entrainment zone and free troposphere were characterized with extremely low  $S_{\text{tot}}$  values.  
 769 Figure 5 presents the spatial distribution of  $N_{3-10}$  particle concentrations along the flight path at ~1,200 m altitude  
 770 (dashed lines in Figs. 4b–d), with the calculated vertical turbulent fluxes labeled at their respective measurement  
 771 locations. Concentrations up to  $10,000 \text{ cm}^{-3}$  were observed along the flight track, with the highest values concentrated  
 772 within a horizontal extent of less than 10 km. The substantial downward fluxes of  $N_{3-10}$  particles ( $-41,092$  and  $-2,975$   
 773  $\text{cm}^{-2} \text{ s}^{-1}$ ) at ~1,200 m both exceed their respective limits of detection (Table 1), confirming that the observed downward  
 774 transport represents a statistically significant atmospheric signal rather than measurement noise. The downward flux

**Deleted:** is likely an artifact due to cloud droplet shattering.

**Formatted:** Font color: Blue

**Formatted:** Font color: Blue

**Formatted:** Font color: Blue

**Deleted:** (Sharp gradients in the potential temperature (orange) profile, often called potential temperature inversion or capping inversion, mark the top of the MBL. These gradients indicate the presence of an entrainment zone (e.g.,

**Deleted:** , a layer at the top of the boundary layer where free tropospheric air masses are entrained into the capping inversion and interact with convective thermals rising from below

**Deleted:** The sharp gradients in mixing ratios shown in Figs. 4b–d indicate moisture convergence that either precedes cloud formation or reflects recently dissipated clouds that have left behind residual moisture signatures due to changing atmospheric conditions. Figure 3 demonstrates frequent cloud encounters during this flight.

**Deleted:**

**Deleted:** (

**Deleted:** ,

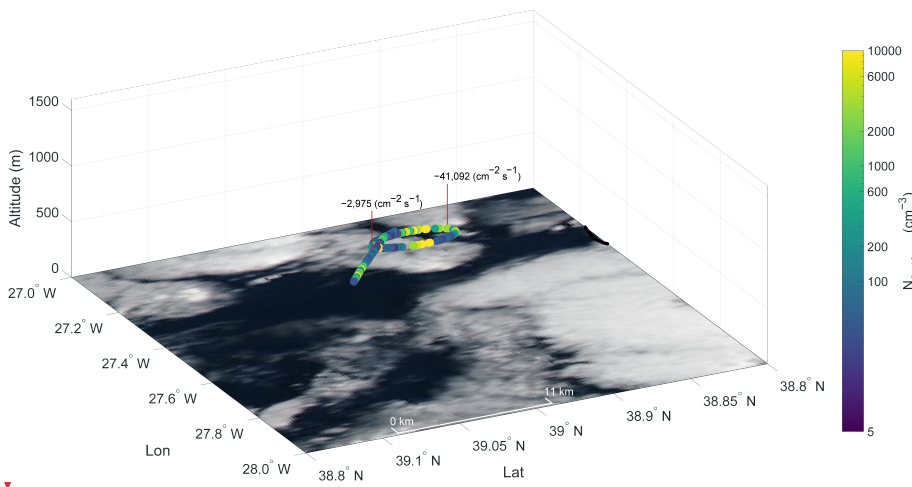
**Deleted:** Zheng et al. (2021)

**Deleted:** ¶

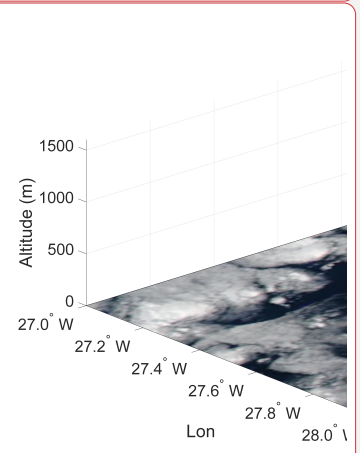
**Deleted:**

794 direction indicates that the source of freshly nucleated particles was located above the measurement altitude, within  
 795 the entrainment zone, while the large difference in flux magnitudes between the two events likely reflects spatial  
 796 heterogeneity in source strength and the proximity of the aircraft to the nucleation zone during each transect. This  
 797 interpretation is supported by the near-absence of  $N_{3-10}$  at  $\sim 1,600$  m during 11:14–11:25 and 12:51–13:01 UTC (Fig.  
 798 3), with the exception of brief concentration spikes of uncertain origin retained in the record due to insufficient  
 799 evidence for their removal. The small particle size (3–10 nm) and limited horizontal extent of less than 10 km further  
 800 argue against a free tropospheric nucleation source, as particles originating in the free troposphere would be expected  
 801 to have grown substantially and the plume to have diluted during descent to measurement altitude. Several mechanisms  
 802 could promote nucleation specifically within the entrainment zone: adiabatic cooling in the rising convective plumes,  
 803 turbulent fluctuation in temperature and vapor concentration generated by entrainment, and dilution of mixed-layer  
 804 air by the entrained free tropospheric air, causing a sudden reduction in preexisting aerosol surface area (Nilsson et  
 805 al., 2001). The extremely low  $S_{tot}$  values observed in the entrainment zone and free troposphere (Fig. 4), falling well  
 806 below the campaign averages, are consistent with this interpretation. These conditions are analogous to those identified  
 807 in previous studies linking entrainment zone nucleation to reduced condensation sink environments (Größ et al., 2018;  
 808 Meskhidze et al., 2019; Nilsson et al., 2001). Supplementary Figs. S9 and S10 provide additional support, showing a  
 809 downward flux of  $N_{3-10}$  particles ( $-1,195 \text{ cm}^{-2} \text{ s}^{-1}$ ) at 1,375 m with complete absence of  $N_{3-10}$  above  $\sim 1,400$  meters,  
 810 consistent with SPE occurrence specifically within the entrainment zone between 1,375–1,400 m.  
 811 Figures 3–5 and the flux analysis (Table 1) demonstrate that the entrainment zone nucleation near the MBL top  
 812 occurred on two days (January 29 and February 10, 2018), representing nearly 5% of flight days. Despite a relatively  
 813 small horizontal extent ( $<10$  km), these newly formed particles can be entrained in the boundary layer via vertical  
 814 turbulent processes, potentially playing an important role in marine aerosol number budget and, given sufficient time  
 815 for growth to CCN-relevant sizes, potentially influencing cloud condensation nuclei concentrations for marine  
 816 stratocumulus clouds.

- Deleted:** Previous studies identify the mixed layer or entrainment zone as the likely location for nucleation events
- Deleted:** that
- Deleted:** initiate
- Deleted:** include
- Deleted:** caused
- Deleted:** flux
- Deleted:** decrease
- Deleted:** concentration
- Deleted:** (Größ et al., 2018; Meskhidze et al., 2019; Nilsson et al., 2001)



**Deleted:** Combined with extremely low preexisting particle concentrations, these processes create favorable conditions for new particle formation. <sup>†</sup>



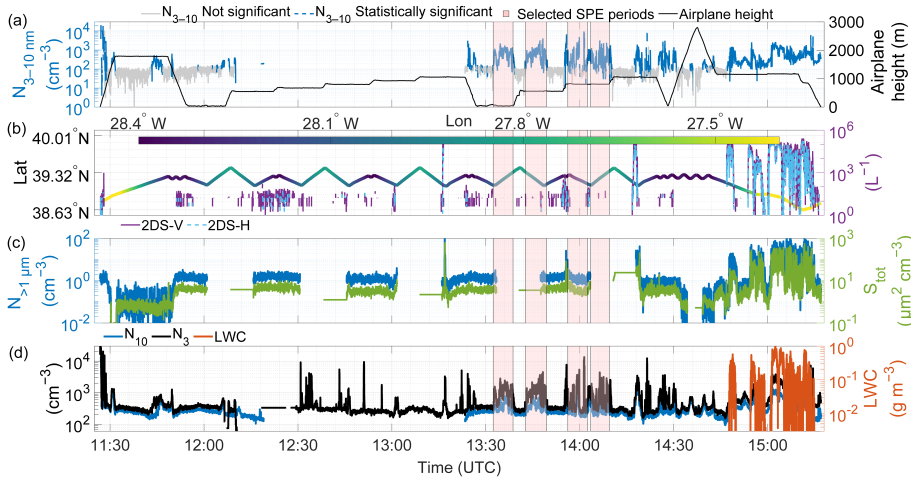
**Deleted:**

817

833 **Figure 5. Spatial distribution of  $N_{3-10}$  particle concentrations along the flight track at ~1,200 m altitude during the period**  
 834 **highlighted in Figures 3 and 4. Calculated vertical turbulent fluxes are labeled at their respective measurement locations.**  
 835 **Color scale indicates  $N_{3-10}$  particle number concentrations ( $\text{cm}^{-3}$ ). The background shows a true-color satellite-corrected**  
 836 **reflectance image from the overpass at 15:15 UTC, with the ocean surface appearing dark and clouds appearing white.**  
 837 **Credit: NASA Worldview Snapshots.**

838 **Case 2: SPE occurring at the interface between the well-mixed surface layer and the decoupled layer**

839 **Figures 6–8 present data from June 21, 2017, with additional examples from July 7, 2017, February 18, 2018 and**  
 840 **February 12, 2018, shown in Supplementary Figs. S11–S13, S14–16, and S17–S19. Back-trajectory analysis (not**  
 841 **shown) indicates that the sampled air masses originated from the Arctic and were therefore expected to be relatively**  
 842 **clean. Figure 6 covers approximately 4 hours of flight operations, during which the aircraft initially flew at very low**  
 843 **altitudes (~30 and 50 m) near 12:00 and 13:30 UTC before gradually ascending to ~1,000 m. Drizzle number**  
 844 **concentration by 2DS (purple and blue lines in Fig. 6b) was absent or below the threshold during the selected SPE**  
 845 **periods. Multiple events with  $N_{3-10}$  concentrations from  $10^2$  to  $10^4 \text{ cm}^{-3}$  were observed throughout the second half of**  
 846 **the flight. The flight trajectory (Fig. 6b) reflects predominantly east-west movement, spanning latitudes from**  
 847 **approximately  $38.6^\circ$  to  $39.3^\circ\text{N}$  and longitudes from  $-28.4^\circ$  to  $-27.4^\circ\text{W}$ . Pink-highlighted intervals show periods with**  
 848 **concurrent increases in  $N_3$  and  $N_{10}$  concentrations exceeding  $10^3 \text{ cm}^{-3}$ , indicative occurrences of SPEs. As in Case 1,**  
 849 **supermicron particle concentrations (blue in Fig. 6c) and total particle surface area (green in Fig. 6c) remained low**  
 850 **during the selected SPE periods, indicating the absence of coarse-mode particles such as sea spray.**



851 **Figure 6. Same as Figure 3 but for June 21, 2017. Gaps in the time series indicate the missing data.**

853 **Figure 7a shows size-resolved particle number concentrations evolution during 13:30–14:20 UTC, encompassing the**  
 854 **four pink-highlighted intervals from Fig. 6. The panel Fig. 7a displays  $N_{3-10}$  particle concentrations. High  $N_{3-10}$**   
 855 **concentrations were encountered at multiple altitudes, with maximum values exceeding  $1,800 \text{ cm}^{-3}$  at ~800 m.**

**Formatted: Font: 9 pt, Bold**

**Formatted: Space After: 12 pt, Line spacing: single**

**Formatted: Font: 9 pt**

**Deleted: Figure 5. Spatial distribution of  $N_{3-10}$  particle concentrations along the flight track during the period highlighted in Figures 3 and 4. Calculated vertical turbulent Mean calculated fluxes are labeled at their respective measurement locations on the track. Color scale indicates  $N_{3-10}$  particle number concentrations ( $\text{cm}^{-3}$ ). The background shows a true-color satellite-corrected reflectance image taken from the overpass at 15:15 UTC, with the ocean surface appearing dark and clouds appearing white., Credit: NASA Worldview Snapshots.**

**The exact spatial location and the horizontal extent of the SPE cannot be definitely determined from aircraft measurements alone. However, substantial downward flux of  $N_{3-10}$  particles ( $-41,092$  and  $-2,975 \text{ cm}^{-2} \text{ s}^{-1}$ ) at ~1,200 m strongly suggests nucleation occurring within the entrainment zone. This interpretation is supported by the absence of  $N_{3-10}$  at ~1,600 m during 11:14–11:25 and 12:51–13:01 UTC (Fig. 3). The small particle size (3–10 nm) and less than 10 km horizontal extent argue against free tropospheric nucleation, as particles would have grown and the plume would have diluted during descent. Supplementary Figs. S8 and S9 show a downward flux of ... [2]**

**Formatted**

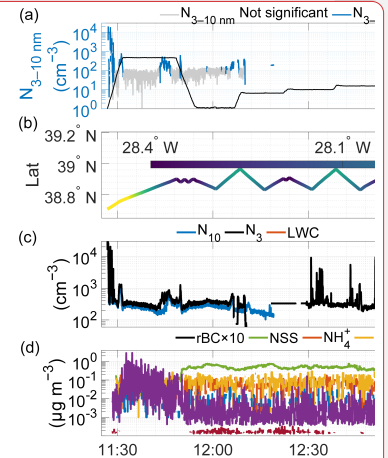
**Deleted: 0**

**Deleted: 2... S143...165... and S176...S198**

**Formatted: Font color: Blue**

**Formatted**

**Deleted: Figures 6–8 present data from June 21, 2017 (with additional examples from July 7, 2017, February 18, 2018 and February 12, 2018 shown in Supplementary Figs. S10–S12, S13–15, and S16–S18). Figure 6 shows approximately 4 hours of flight ... [6]**



**Deleted:**

**Deleted:**

**Formatted: Caption, Space After: 12 pt**

1010 The potential temperature and water vapor profiles (Figs. 7b,c) show the MBL structure consisting of a well mixed  
1011 surface layer extending to  $\sim 700$  m and a decoupled upper boundary layer between  $\sim 700$ – $1300$  m. Decoupled  
1012 structures typically form from radiative heating of the cloud layer and evaporative cooling in the sub-cloud layer,  
1013 which stabilize the boundary layer and suppress vertical mixing (Galewsky et al., 2022; Jones et al., 2011; Wood and  
1014 Bretherton, 2004). Sharp gradients in both potential temperature and mixing ratio around  $1,300$  m marking the  
1015 entrainment zone, above which the free troposphere begins above  $1,400$  m. The  $(\sigma_w^2 w_*^{-2})$  profiles show higher  
1016 magnitudes in the mixed layer (indicating active turbulence) and low magnitudes in both the decoupled layer (due to  
1017 stratification and suppressed vertical mixing) and free troposphere. Total particle surface area remained low in the  
1018 mixed layer but increased considerably toward the top of the mixed layer before decreasing in the decoupled layer and  
1019 reaching very low values in the free troposphere.  
1020

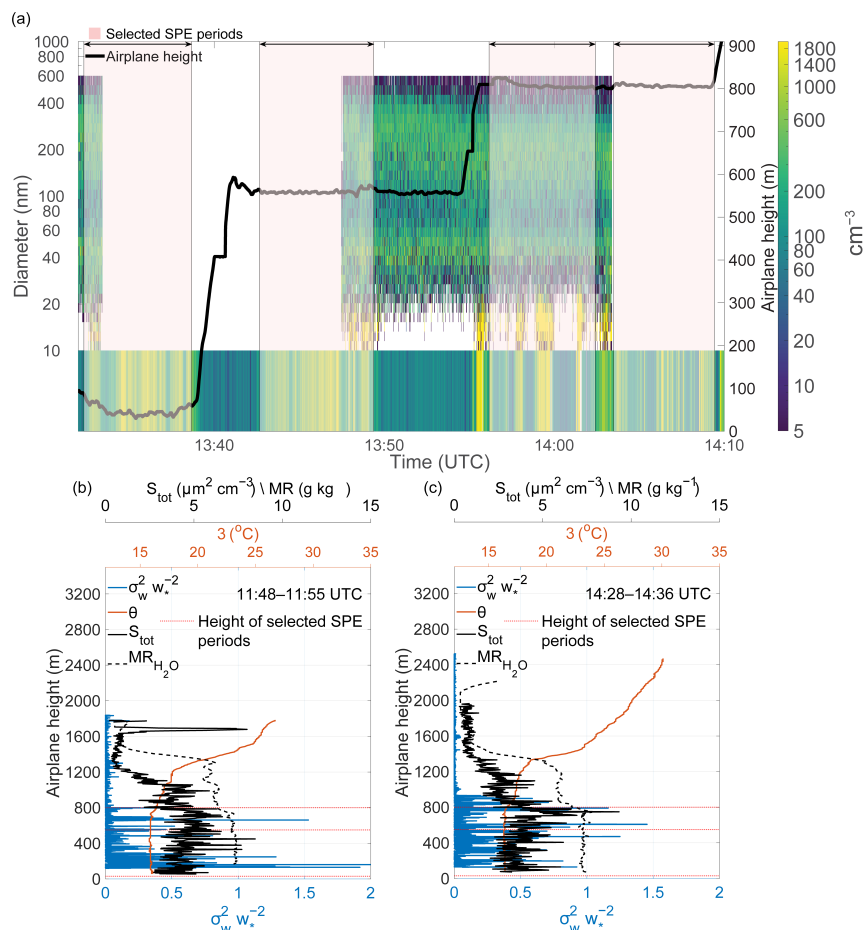


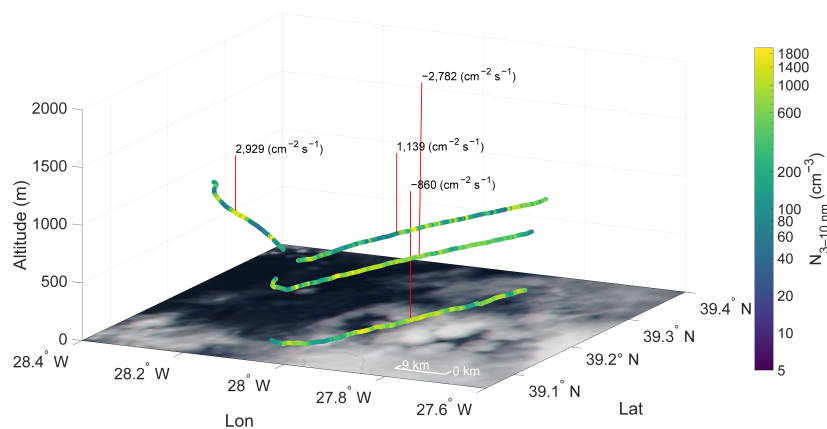
Figure 7. Same as Figure 4, but for June 21, 2017. Gaps in the time series indicate the missing data

Formatted: Font color: Blue

1021  
1022  
1023  
1024  
1025  
1026  
1027  
1028  
1029  
1030

Figure 8 shows  $N_{3-10}$  particle concentrations along flight paths at varying altitudes: 30 m, 550 m, and two segments at 800 m. We separated the 800 m path to prevent the airplane sampling the same air mass because from 13:55–14:03 UTC the aircraft flew along the prevailing wind direction, then changed direction by  $90^\circ$  to fly perpendicular to the wind. The positive vertical turbulent fluxes at 800 and negative values below suggest the SPE occurred between 550–800 meters, likely at the top of the well mixed layer or the bottom of the decoupled layer. The nucleation processes in the entrainment zone and at the base of the decoupled layer could be mechanically similar. Both locations feature the convergence of distinct air masses, in this case, the well-mixed surface layer and

1031 the stratified decoupled layer above, which generates turbulent mixing and aerosol dilution effects. While less  
 1032 pronounced than at the boundary layer top, the interface between these layers exhibits comparable thermodynamic  
 1033 conditions: potential temperature gradients, contrasting vapor concentrations, and localized adiabatic cooling. Figure  
 1034 7 demonstrates that the decoupled layer maintains significantly lower aerosol surface area concentrations relative to  
 1035 the well-mixed layer below, establishing conducive conditions for nucleation when air mass mixing occurs. A key  
 1036 distinction, however, lies in the spatial characteristics, whereas entrainment zone nucleation showed limited horizontal  
 1037 extent (<10 km), the decoupled layer event spanned at least 50–60 km, suggesting either more persistent favorable  
 1038 conditions or a fundamentally different source mechanism operating over regional scales.



039 **Figure 8. Spatial distribution of  $N_{3-10}$  particle concentrations along the flight track at varying altitudes (30 m, 550 m, and**  
 040 **800 m) during the period highlighted in Figures 6 and 7. Calculated vertical turbulent fluxes are labeled at their respective**  
 041 **measurement locations. Color scale indicates  $N_{3-10}$  particle number concentrations ( $\text{cm}^{-3}$ ). The background shows a true-**  
 042 **color satellite reflectance image from the overpass at 14:15 UTC, with the ocean surface appearing dark and clouds**  
 043 **appearing white. Credit: NASA Worldview Snapshots.**  
 044

045 **Figure 8 reveals a strong negative flux of  $N_{3-10}$  ( $-2,782 \text{ cm}^{-2} \text{ s}^{-1}$ ) at 550 m that is nearly three times greater**  
 046 **in magnitude than the flux at 50 m ( $-860 \text{ cm}^{-2} \text{ s}^{-1}$ ), likely due to particle evolution through growth and coagulation,**  
 047 **and dilution processes during vertical transport. The positive fluxes of  $N_{3-10}$  observed at 800 m ( $2,929$  and  $1,139 \text{ cm}^{-2}$**   
 048  **$\text{s}^{-1}$ ) suggest that nucleation initiated either at the top of the well-mixed boundary layer or at the bottom of the overlying**  
 049 **decoupled layer. This bidirectional flux structure suggests that newly formed particles were transported both upward**  
 050 **and downward from the formation zone through turbulent mixing. The comprehensive analysis presented in Figs. 6–**  
 051 **8, combined with the flux calculations in Table 1, provides some evidence that SPEs can originate within decoupled**  
 052 **layer structures, constituting a significant source of secondary marine aerosols in stratified boundary layer conditions.**

Formatted: Normal, Space Before: 12 pt, After: 12 pt

Deleted: ¶

Deleted: Figure 8. Spatial distribution of  $N_{3-10}$  particle concentrations along the flight track at varying altitudes (30 m, 550 m, and 800 m) during the period highlighted in Figures 6 and 7. Calculated vertical turbulent fluxes are labeled at their respective measurement locations. Color scale indicates  $N_{3-10}$  particle number concentrations ( $\text{cm}^{-3}$ ). The background shows a true-color satellite reflectance image from the overpass at 14:15 UTC, with the ocean surface appearing dark and clouds appearing white. Credit: NASA Worldview Snapshots. Same as Figure 3, but for June 21, 2017. The background shows a satellite-corrected reflectance image taken from the overpass at 14:15 UTC with the ocean surface appearing dark and clouds appearing white. Credit: NASA Worldview Snapshots. ¶

067 **4. Discussion**

068 This study demonstrates the value of vertical turbulent flux measurements for characterizing small particle events  
069 (SPE) in remote marine boundary layers. By deriving 3–10 nm particle fluxes from aircraft measurements during the  
070 ACE-ENA campaign, we identified two mechanistically distinct SPE scenarios that challenge conventional  
071 understanding of marine aerosol sources. Critically, while flux sign alone identifies the vertical location of the particle  
072 source, flux magnitude serves two additional essential roles: first, it must exceed the limit of detection to confirm that  
073 the observed directional transport represents a statistically significant atmospheric signal rather than measurement  
074 noise; and second, it provides quantitative constraints on source strength that cannot be obtained from sign alone.

075 Our analysis reveals different SPE mechanisms operating in the marine boundary layer. The first mode – entrainment  
076 zone nucleation – occurs at the boundary layer top (1,200–1,400 m) where several factors create favorable conditions:  
077 (1) dilution of mixed-layer air by entrained free tropospheric air causes sudden decreases in preexisting aerosol surface  
078 area, (2) adiabatic cooling in rising convective plumes reduces saturation vapor pressures, and (3) turbulent  
079 fluctuations in temperature and vapor concentration enhance nucleation rates (Größ et al., 2018; Nilsson et al., 2001).  
080 Strong downward fluxes (up to  $-41,092 \text{ cm}^{-2} \text{ s}^{-1}$ ) exceeding the limit of detection confirm that nucleation occurs  
081 specifically within this ~200 m entrainment layer, while the absence of 3–10 nm particles above the entrainment zone  
082 rules out a free tropospheric source. The limited horizontal extent (2–9 km) of these events is consistent with the  
083 spatial scales of organized convective structures that develop in the upper decoupled marine boundary layer following  
084 cold front passages in the Azores region, where cumulus-associated drizzle reduces the condensation sink to levels  
085 favorable for nucleation (Etling and Brown, 1993; Zheng et al., 2021).

086 The large difference in flux magnitudes between the two entrainment zone events ( $-41,092$  vs.  $-2,975 \text{ cm}^{-2} \text{ s}^{-1}$ )  
087 provides information that flux sign alone cannot supply: it reflects spatial heterogeneity in source strength and the  
088 proximity of the aircraft to the nucleation zone during each transect. As turbulent intensity is unlikely to have changed  
089 substantially over the ~1–2 hour interval separating the two transects, the order-of-magnitude difference in flux  
090 magnitude more plausibly reflects variation in the horizontal distance between the aircraft and the nucleation zone, or  
091 spatial heterogeneity in source strength, rather than a change in the turbulent transport efficiency itself. These flux  
092 magnitudes, integrated over the duration of the events, represent a substantial source of freshly nucleated particles to  
093 the marine aerosol number budget, constraints that can be used directly to evaluate nucleation parameterizations in  
094 regional and global models. While the ultimate contribution of these particles to CCN populations depends on growth  
095 timescales and loss processes during vertical transport (requiring ~24–48 hours at typical marine growth rates of ~1  
096 nm hr<sup>-1</sup> to reach CCN-relevant sizes; (Zheng et al., 2021)), the flux-based constraints provided here represent a  
097 necessary observational foundation for quantifying this contribution in future studies. Our analysis reveals a second  
098 distinct mode of SPE occurring within decoupled marine boundary layer structures, where particles originate at the  
099 interface between the well-mixed surface layer and the overlying decoupled layer (~700–800 m altitude). Unlike  
100 entrainment zone nucleation, which occurs at the boundary layer top, decoupled layer nucleation operates within the  
101 interior of the boundary layer at the interface between the well-mixed surface layer and the overlying stratified layer.  
102 Both mechanisms share key preconditions: convergence of air masses with contrasting thermodynamic properties.

Deleted: ¶

Deleted: ¶

Formatted: Font color: Blue

Deleted: new particle formation (NPF)

Deleted: NPF

Formatted: Font color: Blue

Deleted: NPF

Formatted: Font color: Blue

Deleted: and

Deleted: provide direct evidence that nucleation occurs specifically in this ~200 m layer

Deleted: The limited horizontal extent (2–9 km) of these events

Deleted: . comparable to the wavelength-to-depth ratios of convective roll vortices (Etling and Brown, 1993; Hartmann et al., 1997), suggests that organized boundary layer convection may concentrate precursor vapors and newly formed particles into coherent structures.¶

Deleted: new particle formation

Formatted: Font color: Blue

1118 gradients in potential temperature and water vapor mixing ratio, and aerosol dilution that suppresses the condensation  
1119 sink. However, the decoupled layer mode is distinguished by stratified vertical mixing that confines turbulent  
1120 exchange to a narrower altitude range. It is also characterized by a substantially larger horizontal extent (>50 km)  
1121 compared to entrainment zone events (<10 km), suggesting either more persistent favorable conditions or a  
1122 fundamentally different source mechanism operating at regional scales. This mode exhibits a regional-scale horizontal  
1123 extent (>50 km) compared to the localized nature (<10 km) of entrainment zone events. The substantial negative flux  
1124 magnitudes observed at intermediate altitudes ( $-2,782 \text{ cm}^{-2} \text{ s}^{-1}$  at 550 m) combined with positive fluxes aloft  
1125 demonstrate active particle redistribution throughout the marine boundary layer. The factor of ~3 difference in flux  
1126 magnitude between the 550 m and 30 m levels ( $-2,782$  vs.  $-860 \text{ cm}^{-2} \text{ s}^{-1}$ ) is consistent with attenuation of the particle  
1127 flux during downward transport through dilution with ambient air, as well as losses through coagulation and growth  
1128 out of the 3–10 nm size range. This vertical divergence in flux magnitude represents a quantitative signature of particle  
1129 evolution during transport that flux sign alone would be incapable of revealing. This mode represents a significant and  
1130 previously underappreciated source of secondary marine aerosols that can efficiently contribute to regional aerosol  
1131 budgets through direct incorporation into the surface mixed layer where particles undergo growth to cloud-relevant  
1132 sizes.

**Deleted:** While mechanically similar to entrainment zone processes through air mass convergence, thermodynamic gradients, and aerosol dilution effects, decoupled layer nucleation occurs within the boundary layer structure rather than at its top, operating under conditions of reduced aerosol surface area concentrations and stratified vertical mixing.

**Deleted:** , suggesting t

**Deleted:** cloud condensation nuclei

**Formatted:** Font color: Blue

## 1133 5. Conclusions

1134 The occurrence of newly formed particles in marine environments has been documented in a number of previous  
1135 studies. Wiedensohler et al., (1996) observed sub-20 nm particles originating from the free troposphere or cloud tops  
1136 within the MBL and mixed downwards over the open ocean, suggesting in-situ production based on correlations with  
1137 absolute humidity. Covert et al., (1992) reported sub-20 nm particle production near precipitating cloud tops within  
1138 the MBL, where larger particles acting as condensation sinks had been scavenged by precipitation, with sub-20 nm  
1139 particles dominating 10% of the campaign and indicating episodic rather than continuous production. O'Dowd et al.,  
1140 (2002) documented NPF events at the coastal Mace Head station when marine air masses encountered biogenic  
1141 emissions from the intertidal zone. The ACORES campaign, conducted over the Azores at the same time as ACE-  
1142 ENA, reported freshly nucleated particle bursts near the cloud top exceeding background MBL concentrations by  
1143 more than an order of magnitude (Siebert et al., 2021). Concurrent helicopter-borne particle flux measurements over  
1144 the Azores during ACORES (Lückerath et al., 2022) also documented particle fluxes in the marine boundary layer,  
1145 providing complementary observational context to our aircraft-based approach. The prevailing theoretical framework,  
1146 based on relatively high sea spray aerosol surface area acting as condensation and coagulation sinks (Bates et al.,  
1147 1998; Pirjola et al., 2000), nonetheless predicted that NPF should rarely occur in remote marine boundary layers over  
1148 open oceans. Our flux-based observations build on this existing framework by providing the first direct constraints on  
1149 the vertical source location and strength of freshly nucleated particles in the remote marine boundary layer. Low  
1150 aerosol surface area and specific meteorological configurations can create localized or regional zones where conditions  
1151 become favorable. For entrainment zone and decoupled layer events, extremely low aerosol concentrations, combined  
1152 with turbulent mixing and adiabatic cooling can create a transient "window" where nucleation can proceed despite  
1153 moderate surface area concentrations lower in the boundary layer. Recent ground-based observations from the same

**Deleted:** (

**Deleted:** (

**Deleted:** (

**Deleted:** The prevailing theoretical framework, based on relatively high sea spray aerosol surface area acting as condensation and coagulation sinks (Bates et al., 1998; Pirjola et al., 2000), predicted that NPF should rarely occur in remote marine boundary layers over open oceans. Our observations demonstrate that this framework is incomplete...

1171 campaign (Zheng et al., 2021), documented frequent NPF events but could not definitively determine vertical location.  
 1172 Our flux-based approach resolves this ambiguity by providing direct evidence of where particles originate relative to  
 1173 the measurement location. The negative (downward) fluxes in Case 1 unambiguously demonstrate an above-aircraft  
 1174 source, while the bidirectional fluxes in Case 2 indicate a distributed source encompassing the measurement altitude.

1175 These findings have important implications for understanding marine aerosol budgets. The spatial scales of these two  
 1176 SPE modes differ by an order of magnitude: entrainment zone events exhibited limited horizontal extents (<10 km),  
 1177 consistent with localized convective structures, while decoupled layer events spanned regional scales (50-60 km),  
 1178 suggesting fundamentally different formation mechanisms or persistence of favorable conditions. For the entrainment  
 1179 zone mode, while the aircraft sampled the SPE for only ~4 minutes during each transect due to its high ground speed,  
 1180 NPF events in marine and continental environments are typically observed to persist for 2–5 hours (Islam et al., 2022;  
 1181 Kulmala et al., 2004; Zheng et al., 2021). Assuming the measured downward flux of  $-41.092 \text{ cm}^{-2} \text{ s}^{-1}$  is representative  
 1182 of a nucleation event of typical duration of ~3 hours and using a mixed layer depth of ~1,200 m, the estimated increase  
 1183 in vertically integrated particle number concentration is approximately:

$$1184 \Delta N_{3-10} \approx |F| \times \frac{\Delta t}{z_{MBL}} = \frac{41,092 \times 10,800}{1.2 \times 10^5} \approx 3,700 \text{ cm}^{-3}$$

1185 where  $F$  is the flux in  $\text{cm}^{-2} \text{ s}^{-1}$ ,  $\Delta t$  is the event duration in seconds, and  $z_{MBL}$  is the mixed layer depth in cm. This  
 1186 represents a substantial addition to the total particle number concentration in the surface mixed layer, noting that this  
 1187 estimate refers to freshly nucleated 3–10 nm particles rather than CCN-relevant particles. The fraction surviving to  
 1188 CCN-relevant sizes (>50–80 nm) depends on growth rates and loss processes that cannot be quantified from single  
 1189 aircraft transects alone. However, Zheng et al. (2021) estimated that under favorable conditions at the same site, newly  
 1190 formed particles contributed on average ~50% of total CCN concentrations following cold front passages, suggesting  
 1191 that even accounting for coagulation losses, the contribution of entrainment zone nucleation to the marine CCN budget  
 1192 may be substantial. Entrainment zone nucleation, despite its limited horizontal extent, may contribute significantly to  
 1193 the marine aerosol number budget through sustained downward transport via convective mixing. Though flux  
 1194 magnitudes for the decoupled layer nucleation events ( $-2,782 \text{ cm}^{-2} \text{ s}^{-1}$ ) are less pronounced, their large spatial extent  
 1195 likely results in comparable or larger aggregate contributions to regional aerosol budgets. We note that the contribution  
 1196 of freshly nucleated particles to CCN population depends on growth rates and loss processes during transport and  
 1197 cannot be assessed from short-term measurements alone. The flux magnitudes and vertical source locations reported  
 1198 here provide the observational foundation needed to evaluate this contribution quantitatively in future studies  
 1199 combining particle flux measurements with growth rate and CCN closure analyses.

1200 Our observations, combined with combined with the longer history of marine NPF observations cited above and recent  
 1201 ground-based measurements from the same campaign (Zheng et al., 2021), suggest that the contribution of in-situ  
 1202 marine boundary layer nucleation to the aerosol budget may be more significant than current model representations  
 1203 assume. Climate models have historically followed theoretical expectations that marine boundary layer nucleation  
 1204 should be negligible, instead representing new particles as primarily originating from free tropospheric entrainment  
 1205 or long-range continental transport (Clarke et al., 2013; Logan et al., 2014), with marine boundary layer nucleation  
 1206 treated as negligible. The frequent occurrence of SPE during the ACE-ENA campaign (entrainment zone nucleation  
 1207 in 2 and decoupled layer nucleation in 4 of 39 flights analyzed) suggests that marine boundary layer nucleation – in

Deleted: (Zheng et al., 2021)

Deleted: CCN

Deleted: Notably,

Deleted: t

Deleted: NPF

Deleted: (

Deleted: ,

Deleted: Entrainment zone nucleation, despite limited horizontal extent, may contribute significantly to CCN populations through sustained downward transport via convective mixing. The calculated flux of  $-41,092 \text{ cm}^{-2} \text{ s}^{-1}$  integrated over several hours could deliver substantial numbers of particles to the surface mixed layer where they can grow to CCN sizes. Though flux magnitudes for the decoupled layer nucleation events ( $-2,782 \text{ cm}^{-2} \text{ s}^{-1}$ ) are less pronounced, their large spatial extent likely makes even larger contributions to regional CCN budgets.

Moved (insertion) [2]

Deleted: demonstrate that this representation misses an important aerosol source.

Moved up [2]: Climate models have historically followed theoretical expectations that marine boundary layer nucleation should be negligible, instead representing new particles as primarily originating from free tropospheric entrainment or long-range continental transport (Clarke et al., 2013; Logan et al., 2014)

Deleted: .

Deleted: NPF events

1233 both modes – may be more climatologically important than previously recognized. Given that marine boundary layer  
1234 cloud microphysical properties exhibit the highest sensitivity to aerosol changes (Bellouin et al., 2020; Zhang et al.,  
1235 2024), and that even modest changes in CCN concentrations can substantially affect cloud radiative forcing in these  
1236 pristine environments, proper representation of NPF sources is critical for reducing uncertainties in aerosol-cloud  
1237 interaction estimates.

1238 The continuous wavelet transform (CWT) approach proved essential for deriving reliable fluxes from fast-moving  
1239 aircraft platforms. Traditional eddy covariance methods require stationarity conditions that are difficult to maintain  
1240 during aircraft sampling, where the platform continuously moves through different air masses. The CWT method's  
1241 ability to handle non-stationary data while avoiding systematic errors from linear detrending (Rannik and Vesala,  
1242 1999; Schaller et al., 2017) enabled flux calculations even during complex meteorological conditions. Our detailed  
1243 analysis of frequency response and flux loss corrections demonstrates that 1 Hz CPC measurements, while not ideal,  
1244 can resolve sufficient turbulent scales to capture the dominant flux contributions when proper corrections are applied.

1245 Importantly, flux magnitudes (not just flux sign) provide essential scientific value: they must exceed the limit of  
1246 detection to confirm statistical significance, they constrain source strength and proximity, and they provide  
1247 quantitative inputs for evaluating nucleation parameterizations in regional and global models. As the scientific  
1248 community works to reduce uncertainties in aerosol-cloud interactions, flux-based approaches offer a promising path  
1249 forward for understanding how, where, and when new particles form in Earth's remote marine atmosphere.

1250 Several limitations warrant acknowledgment. First, our 3–10 nm size range likely misses the initial nucleation at  
1251 molecular cluster sizes (~1–3 nm), meaning we observe "small particle events" rather than nucleation itself. However,  
1252 the rapid appearance of 3–10 nm particles with clear vertical structure in turbulent fluxes provides strong indirect  
1253 evidence for nearby nucleation. Second, the aircraft's high ground speed (~100 m s<sup>-1</sup>) compared to typical tower-based  
1254 measurements introduces challenges for capturing the full turbulent spectrum, particularly at lower altitudes where  
1255 eddy sizes are smaller. Our flux loss corrections ( $F_m/F$  ratios of 0.70–0.99) account for this limitation but introduce  
1256 additional uncertainty. Third, we cannot determine definitively the exact horizontal extent of NPF events from single  
1257 aircraft transects, though crosswind sampling provides minimum extent estimates.

## 1258 **Future Directions**

1259 This work establishes aircraft-derived aerosol fluxes as a valuable tool for characterizing marine boundary layer  
1260 aerosol sources. Several directions would advance understanding:

1261 **Slower aircrafts:** Unmanned aerial vehicles operating at 30–40 m s<sup>-1</sup> would better resolve small-scale turbulence,  
1262 particularly near the surface, where flux loss corrections are currently largest, improving flux accuracy and enabling  
1263 more detailed vertical structure analysis.

1264 **Expanded measurements:** Simultaneous flux measurements of precursor gases (H<sub>2</sub>SO<sub>4</sub>, NH<sub>3</sub>, amines, organics)  
1265 would directly test hypotheses about nucleation mechanisms and identify which chemical pathways dominate in  
1266 different scenarios.

Formatted: Font: Italic

1267 **Multi-aircraft coordination:** Coordinated measurements from more than one aircraft at different altitudes could  
1268 directly observe vertical particle transport rates and evolution, constraining growth rates and loss processes during  
1269 transit.

1270 **Longer-term statistics:** Expanding beyond campaign-based measurements to seasonal or annual timescales would  
1271 quantify the climatological importance of different NPF modes and their relationships to synoptic meteorological  
1272 patterns.

1273 **Model evaluation:** Using observed flux [magnitudes and vertical source locations](#) as benchmarks for evaluating marine  
1274 boundary layer nucleation parameterizations in regional and global models would improve their representation of  
1275 aerosol-cloud interactions [and reduce uncertainties in aerosol indirect forcing estimates](#).

Deleted: es

Deleted: .

#### 1276 **Code availability**

1277 All the scripts used to make the figures used in this study will be available along with the supplementary information

#### 1278 **Data availability**

1279 All data from the ACE-ENA campaign are archived at the DOE ARM data center, covering measurements from the  
1280 ARM Aerial Facility near ARM ENA site on Graciosa Island (June 15, 2017 - February 28, 2018).

1281 ARM Aerial Facility (AAF) Merged VAP, <https://doi.org/10.5439/1999133>, (AAFMERGED, (Mei and Gaustad,  
1282 2024)

1283 ARM Aerial Facility (AAF) Merged aerosol size distribution, <https://doi.org/10.5439/1905541>,  
1284 (AAFMERGEDAEROSOLS,(Pekour and Ermold, 2017)

1285 ARM Aerial Facility Isokinetic Inlet, <https://doi.org/10.5439/1241544>, (AAFINLETISOK, (Koontz et al., 2016)

1286 ARM Aerial Facility (AAF) Aircraft Integrated Meteorological Measurement System (AIMMS) - Meteorological  
1287 data, <https://doi.org/10.5439/1349241>, (AAFMETAIMS,(Matthews and Goldberger, 2020)

1288 Interagency Working Group for Airborne Data and Telemetry Systems,  
1289 <https://adc.arm.gov/discovery/#/results/s::aaf%20iwg/iopShortName::aaf2017ace-ena>, (IWG ACEENA)

1290 Proton Transfer Reaction Mass Spectrometer (PTR-MS),  
1291 [https://adc.arm.gov/discovery/#/results/instrument\\_code::ptrms/iopShortName::aaf2017ace-ena](https://adc.arm.gov/discovery/#/results/instrument_code::ptrms/iopShortName::aaf2017ace-ena), (ACE ENA IOP1  
1292 G1 PTRMS)

#### 1293 **Author contribution**

1294 ARS, MDP, and NM conceptualized the study. ARS performed the data curation, formal analysis, and designed the  
1295 figures with contributions from MDP and NM. NM acquired the financial support for the project. ARS and NM wrote  
1296 the paper, and all authors provided input on the paper for revision before submission.

1299 **Competing interests**

1300 The authors declare that they have no conflict of interest.

1301 **Acknowledgements**

1302 We acknowledge the Atmospheric Radiation Measurement (ARM) Climate Research Facility, a user facility of the  
1303 United States Department of Energy (US DOE), Office of Science, sponsored by the Office of Biological and  
1304 Environmental Research. We thank Dr. Jian Wang and all the staff responsible for the operation of the ACE-ENA  
1305 campaign. We acknowledge the use of imagery from the NASA Worldview application, part of the NASA Earth  
1306 Observing System Data and Information System (EOSDIS). AI tools were used to correct the spelling and sentence  
1307 structure of the manuscript

1308 **Financial support**

1309 This work was supported by the DOE Office of Science, Biological and Environment Research, Grant No. DE-  
1310 SC0024873

1311 **References**

- 1312 Andreae, M. O.: Aerosols Before Pollution, *Science*, 315, 50–51, <https://doi.org/10.1126/science.1136529>, 2007.
- 1313 Aubinet, M., Vesala, T., and Papale, D. (Eds.): *Eddy Covariance: A Practical Guide to Measurement and Data*  
1314 *Analysis*, Springer Netherlands, Dordrecht, <https://doi.org/10.1007/978-94-007-2351-1>, 2012.
- 1315 Bates, T. S., Kapustin, V. N., Quinn, P. K., Covert, D. S., Coffman, D. J., Mari, C., Durkee, P. A., De Bruyn, W. J.,  
1316 and Saltzman, E. S.: Processes controlling the distribution of aerosol particles in the lower marine boundary layer  
1317 during the First Aerosol Characterization Experiment (ACE 1), *J. Geophys. Res. Atmospheres*, 103, 16369–16383,  
1318 <https://doi.org/10.1029/97JD03720>, 1998.
- 1319 Bellouin, N., Quaas, J., Gryspeerdt, E., Kinne, S., Stier, P., Watson-Parris, D., Boucher, O., Carslaw, K. S.,  
1320 Christensen, M., Daniau, A. -L., Dufresne, J. -L., Feingold, G., Fiedler, S., Forster, P., Gettelman, A., Haywood, J.  
1321 M., Lohmann, U., Malavelle, F., Mauritsen, T., McCoy, D. T., Myhre, G., Mülmenstädt, J., Neubauer, D., Possner,  
1322 A., Rugenstein, M., Sato, Y., Schulz, M., Schwartz, S. E., Sourdeval, O., Storelvmo, T., Toll, V., Winker, D., and  
1323 Stevens, B.: Bounding Global Aerosol Radiative Forcing of Climate Change, *Rev. Geophys.*, 58, e2019RG000660,  
1324 <https://doi.org/10.1029/2019RG000660>, 2020.
- 1325 Boers, R. and Eloranta, E. W.: Lidar measurements of the atmospheric entrainment zone and the potential temperature  
1326 jump across the top of the mixed layer, *Bound.-Layer Meteorol.*, 34, 357–375, <https://doi.org/10.1007/BF00120988>,  
1327 1986.
- 1328 Carslaw, K. S., Lee, L. A., Reddington, C. L., Pringle, K. J., Rap, A., Forster, P. M., Mann, G. W., Spracklen, D. V.,  
1329 Woodhouse, M. T., Regayre, L. A., and Pierce, J. R.: Large contribution of natural aerosols to uncertainty in indirect  
1330 forcing, *Nature*, 503, 67–71, <https://doi.org/10.1038/nature12674>, 2013.
- 1331 Clarke, A. D., Freitag, S., Simpson, R. M. C., Hudson, J. G., Howell, S. G., Brekhovskikh, V. L., Campos, T.,  
1332 Kapustin, V. N., and Zhou, J.: Free troposphere as a major source of CCN for the equatorial pacific boundary layer:

1333 long-range transport and teleconnections, *Atmospheric Chem. Phys.*, 13, 7511–7529, [https://doi.org/10.5194/acp-13-](https://doi.org/10.5194/acp-13-7511-2013)  
1334 7511-2013, 2013.

1335 Covert, D. S., Kapustin, V. N., Quinn, P. K., and Bates, T. S.: New particle formation in the marine boundary layer,  
1336 *J. Geophys. Res. Atmospheres*, 97, 20581–20589, <https://doi.org/10.1029/92JD02074>, 1992.

1337 Dal Maso, M., Kulmala, M., Riipinen, I., Wagner, R., Hussein, T., Aalto, P. P., and Lehtinen, K.: Formation and  
1338 growth of fresh atmospheric aerosols: eight years of aerosol size distribution data from SMEAR II, Hyttälä, Finland,  
1339 *Boreal Environ. Res.*, 10, 323–336, 2005.

1340 Deardorff, J. W.: Three-dimensional numerical study of turbulence in an entraining mixed layer, *Bound.-Layer*  
1341 *Meteorol.*, 7, 199–226, <https://doi.org/10.1007/BF00227913>, 1974.

1342 Desjardins, R. L., MacPherson, J. I., Schuepp, P. H., and Karanja, F.: An evaluation of aircraft flux measurements of  
1343 CO<sub>2</sub>, water vapor and sensible heat, *Bound.-Layer Meteorol.*, 47, 55–69, 1989.

1344 Dewani, N., Sakradzija, M., Schlemmer, L., Leinweber, R., and Schmidli, J.: Dependency of vertical velocity variance  
1345 on meteorological conditions in the convective boundary layer, *Atmospheric Chem. Phys.*, 23, 4045–4058,  
1346 <https://doi.org/10.5194/acp-23-4045-2023>, 2023.

1347 Ehn, M., Vuollekoski, H., Petäjä, T., Kerminen, V., Vana, M., Aalto, P., de Leeuw, G., Ceburnis, D., Dupuy, R.,  
1348 O’Dowd, C. D., and Kulmala, M.: Growth rates during coastal and marine new particle formation in western Ireland,  
1349 *J. Geophys. Res. Atmospheres*, 115, 2010JD014292, <https://doi.org/10.1029/2010JD014292>, 2010.

1350 Etling, D. and Brown, R. A.: Roll vortices in the planetary boundary layer: A review, *Bound.-Layer Meteorol.*, 65,  
1351 215–248, <https://doi.org/10.1007/BF00705527>, 1993.

1352 Fan, M. and Pekour, M.: CPC\_ACEENA, <https://doi.org/10.5439/1440985>, 2018.

1353 Foken, T., Wimmer, F., Mauder, M., Thomas, C., and Liebethal, C.: Some aspects of the energy balance closure  
1354 problem, *Atmospheric Chem. Phys.*, 6, 4395–4402, <https://doi.org/10.5194/acp-6-4395-2006>, 2006.

1355 Galewsky, J., Jensen, M. P., and Delp, J.: Marine Boundary Layer Decoupling and the Stable Isotopic Composition  
1356 of Water Vapor, *J. Geophys. Res. Atmospheres*, 127, e2021JD035470, <https://doi.org/10.1029/2021JD035470>, 2022.

1357 Gioli, B., Miglietta, F., De Martino, B., Hutjes, R. W. A., Dolman, H. A. J., Lindroth, A., Schumacher, M., Sanz, M.  
1358 J., Manca, G., Peressotti, A., and Dumas, E. J.: Comparison between tower and aircraft-based eddy covariance fluxes  
1359 in five European regions, *Agric. For. Meteorol.*, 127, 1–16, <https://doi.org/10.1016/j.agrformet.2004.08.004>, 2004.

1360 Glienke, S. and Mei, F.: Two-Dimensional Stereo (2D-S) Probe Instrument Handbook,  
1361 <https://doi.org/10.2172/1597436>, 2019.

1362 Größ, J., Hamed, A., Sonntag, A., Spindler, G., Elina Manninen, H., Nieminen, T., Kulmala, M., Hörrak, U., Plass-  
1363 Dülmer, C., Wiedensohler, A., and Birmili, W.: Atmospheric new particle formation at the research station Melpitz,  
1364 Germany: connection with gaseous precursors and meteorological parameters, *Atmospheric Chem. Phys.*, 18, 1835–  
1365 1861, <https://doi.org/10.5194/acp-18-1835-2018>, 2018.

1366 Helbig, M., Gerken, T., Beamesderfer, E. R., Baldochi, D. D., Banerjee, T., Biraud, S. C., Brown, W. O. J., Brunzell,  
1367 N. A., Burakowski, E. A., Burns, S. P., Butterworth, B. J., Chan, W. S., Davis, K. J., Desai, A. R., Fuentes, J. D.,  
1368 Hollinger, D. Y., Kljun, N., Mauder, M., Novick, K. A., Perkins, J. M., Rahn, D. A., Rey-Sanchez, C., Santanello, J.  
1369 A., Scott, R. L., Seyednasrollah, B., Stoy, P. C., Sullivan, R. C., de Arellano, J. V.-G., Wharton, S., Yi, C., and  
1370 Richardson, A. D.: Integrating continuous atmospheric boundary layer and tower-based flux measurements to advance  
1371 understanding of land-atmosphere interactions, *Agric. For. Meteorol.*, 307, 108509,  
1372 <https://doi.org/10.1016/j.agrformet.2021.108509>, 2021.

- 1373 Hoose, C., Kristjánsson, J. E., Iversen, T., Kirkevåg, A., Seland, Ø., and Gettelman, A.: Constraining cloud droplet  
1374 number concentration in GCMs suppresses the aerosol indirect effect, *Geophys. Res. Lett.*, 36, 2009GL038568,  
1375 <https://doi.org/10.1029/2009GL038568>, 2009.
- 1376 Horst, T. W.: A Simple Formula for Attenuation of Eddy Fluxes Measured with First-Order Scalar Sensors, *Bound.-*  
1377 *Layer Meteorol.*, 82, 219–233, <https://doi.org/10.1023/A:1000229130034>, 1997.
- 1378 Intergovernmental Panel on Climate Change (IPCC): *Climate Change 2021 – The Physical Science Basis: Working*  
1379 *Group I Contribution to the Sixth Assessment Report of the Intergovernmental Panel on Climate Change*, 1st ed.,  
1380 Cambridge University Press, <https://doi.org/10.1017/9781009157896>, 2023.
- 1381 Islam, M. M., Meskhidze, N., Rasheeda Satheesh, A., and Petters, M. D.: Turbulent Flux Measurements of the Near-  
1382 Surface and Residual-Layer Small Particle Events, *J. Geophys. Res. Atmospheres*, 127, e2021JD036289,  
1383 <https://doi.org/10.1029/2021JD036289>, 2022.
- 1384 Jones, C. R., Bretherton, C. S., and Leon, D.: Coupled vs. decoupled boundary layers in VOCALS-REx, *Atmospheric*  
1385 *Chem. Phys.*, 11, 7143–7153, <https://doi.org/10.5194/acp-11-7143-2011>, 2011.
- 1386 Kaimal, J. C. and Finnigan, J. J.: *Atmospheric Boundary Layer Flows: Their Structure and Measurement*, Oxford  
1387 University Press, <https://doi.org/10.1093/oso/9780195062397.001.0001>, 1994.
- 1388 Koontz, A., Mei, F., and Pekour, M.: *aafinletisok.a1*, <https://doi.org/10.5439/1241544>, 2016.
- 1389 Korolev, A. and Isaac, G. A.: Shattering during Sampling by OAPs and HVPS. Part I: Snow Particles, *J. Atmospheric*  
1390 *Ocean. Technol.*, 22, 528–542, <https://doi.org/10.1175/JTECH1720.1>, 2005.
- 1391 Kuang, C. and Mei, F.: *Condensation Particle Counter (CPC) Instrument Handbook - Airborne Version*,  
1392 <https://doi.org/10.2172/1562676>, 2019.
- 1393 Kulkarni, P. and Wang, J.: New fast integrated mobility spectrometer for real-time measurement of aerosol size  
1394 distribution: II. Design, calibration, and performance characterization, *J. Aerosol Sci.*, 37, 1326–1339,  
1395 <https://doi.org/10.1016/j.jaerosci.2006.01.010>, 2006a.
- 1396 Kulkarni, P. and Wang, J.: New fast integrated mobility spectrometer for real-time measurement of aerosol size  
1397 distribution—I: Concept and theory, *J. Aerosol Sci.*, 37, 1303–1325, <https://doi.org/10.1016/j.jaerosci.2006.01.005>,  
1398 2006b.
- 1399 Kulmala, M., Vehkamäki, H., Petäjä, T., Dal Maso, M., Lauri, A., Kerminen, V.-M., Birmili, W., and McMurry, P.  
1400 H.: Formation and growth rates of ultrafine atmospheric particles: a review of observations, *J. Aerosol Sci.*, 35, 143–  
1401 176, <https://doi.org/10.1016/j.jaerosci.2003.10.003>, 2004.
- 1402 Kulmala, M., Petäjä, T., Nieminen, T., Sipilä, M., Manninen, H. E., Lehtipalo, K., Dal Maso, M., Aalto, P. P.,  
1403 Junninen, H., Paasonen, P., Riipinen, I., Lehtinen, K. E. J., Laaksonen, A., and Kerminen, V.-M.: Measurement of the  
1404 nucleation of atmospheric aerosol particles, *Nat. Protoc.*, 7, 1651–1667, <https://doi.org/10.1038/nprot.2012.091>, 2012.
- 1405 Lee, X., Massman, W., and Law, B. (Eds.): *Handbook of Micrometeorology: A Guide for Surface Flux Measurement*  
1406 *and Analysis*, Springer Netherlands, Dordrecht, 250 pp., <https://doi.org/10.1007/1-4020-2265-4>, 2005.
- 1407 Lenschow, D. H. and Stankov, B. B.: Length Scales in the Convective Boundary Layer, *J. Atmospheric Sci.*, 43, 1198–  
1408 1209, [https://doi.org/10.1175/1520-0469\(1986\)043<1198:LSITCB>2.0.CO;2](https://doi.org/10.1175/1520-0469(1986)043<1198:LSITCB>2.0.CO;2), 1986.
- 1409 Lenschow, D. H., Wulfmeyer, V., and Senff, C.: Measuring Second- through Fourth-Order Moments in Noisy Data,  
1410 *J. Atmospheric Ocean. Technol.*, 17, 1330–1347, [https://doi.org/10.1175/1520-0426\(2000\)017<1330:MSTFOM>2.0.CO;2](https://doi.org/10.1175/1520-0426(2000)017<1330:MSTFOM>2.0.CO;2), 2000.  
1411

- 1412 Li, Y., Wu, Y., Tang, J., Zhu, P., Gao, Z., and Yang, Y.: Quantitative Evaluation of Wavelet Analysis Method for  
 1413 Turbulent Flux Calculation of Non-Stationary Series, *Geophys. Res. Lett.*, 50, e2022GL101591,  
 1414 <https://doi.org/10.1029/2022GL101591>, 2023.
- 1415 Logan, T., Xi, B., and Dong, X.: Aerosol properties and their influences on marine boundary layer cloud condensation  
 1416 nuclei at the ARM mobile facility over the Azores, *J. Geophys. Res. Atmospheres*, 119, 4859–4872,  
 1417 <https://doi.org/10.1002/2013JD021288>, 2014.
- 1418 Lückerkath, J., Held, A., Siebert, H., Michalkow, M., and Wehner, B.: Vertical aerosol particle exchange in the marine  
 1419 boundary layer estimated from helicopter-borne measurements in the Azores region, *Atmospheric Chem. Phys.*, 22,  
 1420 10007–10021, <https://doi.org/10.5194/acp-22-10007-2022>, 2022.
- 1421 Martin, S., Beyrich, F., and Bange, J.: Observing Entrainment Processes Using a Small Unmanned Aerial Vehicle: A  
 1422 Feasibility Study, *Bound.-Layer Meteorol.*, 150, 449–467, <https://doi.org/10.1007/s10546-013-9880-4>, 2014.
- 1423 Mather, J. H. and Voyles, J. W.: The Arm Climate Research Facility: A Review of Structure and Capabilities, *Bull.*  
 1424 *Am. Meteorol. Soc.*, 94, 377–392, <https://doi.org/10.1175/BAMS-D-11-00218.1>, 2013.
- 1425 Matthews, A. and Goldberger, L.: Aircraft-Integrated Meteorological Measurement System (AIMMS) Instrument  
 1426 Handbook, <https://doi.org/10.2172/1725866>, 2020.
- 1427 Mei, F. and Gaustad, K.: ARM Aerial Facility (AAF) Merged Value-Added Product Report for Historical G-1 Field  
 1428 Campaigns, Oak Ridge National Laboratory (ORNL), Oak Ridge, TN (United States). Atmospheric Radiation  
 1429 Measurement (ARM) Data Center, <https://doi.org/10.2172/2335708>, 2024.
- 1430 Meskhidze, N., Xu, J., Gantt, B., Zhang, Y., Nenes, A., Ghan, S. J., Liu, X., Easter, R., and Zaveri, R.: Global  
 1431 distribution and climate forcing of marine organic aerosol: 1. Model improvements and evaluation, *Atmospheric*  
 1432 *Chem. Phys.*, 11, 11689–11705, <https://doi.org/10.5194/acp-11-11689-2011>, 2011.
- 1433 Meskhidze, N., Jaimes-Correa, J. C., Petters, M. D., Royalty, T. M., Phillips, B. N., Zimmerman, A., and Reed, R.:  
 1434 Possible Wintertime Sources of Fine Particles in an Urban Environment, *J. Geophys. Res. Atmospheres*, 124, 13,055-  
 1435 13,070, <https://doi.org/10.1029/2019JD031367>, 2019.
- 1436 Misztal, P. K., Karl, T., Weber, R., Jonsson, H. H., Guenther, A. B., and Goldstein, A. H.: Airborne flux measurements  
 1437 of biogenic isoprene over California, *Atmospheric Chem. Phys.*, 14, 10631–10647, <https://doi.org/10.5194/acp-14-10631-2014>, 2014.
- 1439 Modini, R. L., Ristovski, Z. D., Johnson, G. R., He, C., Surawski, N., Morawska, L., Suni, T., and Kulmala, M.: New  
 1440 particle formation and growth at a remote, sub-tropical coastal location, *Atmospheric Chem. Phys.*, 9, 7607–7621,  
 1441 <https://doi.org/10.5194/acp-9-7607-2009>, 2009.
- 1442 Nieminen, T., Kerminen, V.-M., Petäjä, T., Aalto, P. P., Arshinov, M., Asmi, E., Baltensperger, U., Beddows, D. C.  
 1443 S., Beukes, J. P., Collins, D., Ding, A., Harrison, R. M., Henzing, B., Hooda, R., Hu, M., Hörrak, U., Kivekäs, N.,  
 1444 Komsaare, K., Krejci, R., Kristensson, A., Laakso, L., Laaksonen, A., Leaitch, W. R., Lihavainen, H., Mihalopoulos,  
 1445 N., Németh, Z., Nie, W., O’Dowd, C., Salma, I., Sellegri, K., Svenningsson, B., Swietlicki, E., Tunved, P., Ulevicius,  
 1446 V., Vakkari, V., Vana, M., Wiedensohler, A., Wu, Z., Virtanen, A., and Kulmala, M.: Global analysis of continental  
 1447 boundary layer new particle formation based on long-term measurements, *Atmospheric Chem. Phys.*, 18, 14737–  
 1448 14756, <https://doi.org/10.5194/acp-18-14737-2018>, 2018.
- 1449 Nilsson, E. D., Rannik, Ü., Kulmala, M., Buzorius, G., and O’Dowd, C. D.: Effects of continental boundary layer  
 1450 evolution, convection, turbulence and entrainment, on aerosol formation, *Tellus Ser. B Chem. Phys. Meteorol. B*, 53,  
 1451 441–461, <https://doi.org/10.3402/tellusb.v53i4.16617>, 2001.
- 1452 Novak, G. A., Fite, C. H., Holmes, C. D., Veres, P. R., Neuman, J. A., Faloona, I., Thornton, J. A., Wolfe, G. M.,  
 1453 Vermeuel, M. P., Jernigan, C. M., Peischl, J., Ryerson, T. B., Thompson, C. R., Bourgeois, I., Warneke, C., Gkatzelis,

- 1454 G. I., Coggon, M. M., Sekimoto, K., Bui, T. P., Dean-Day, J., Diskin, G. S., DiGangi, J. P., Nowak, J. B., Moore, R.  
 1455 H., Wiggins, E. B., Winstead, E. L., Robinson, C., Thornhill, K. L., Sanchez, K. J., Hall, S. R., Ullmann, K., Dollner,  
 1456 M., Weinzierl, B., Blake, D. R., and Bertram, T. H.: Rapid cloud removal of dimethyl sulfide oxidation products limits  
 1457 SO<sub>2</sub> and cloud condensation nuclei production in the marine atmosphere, *Proc. Natl. Acad. Sci.*, 118, e2110472118,  
 1458 <https://doi.org/10.1073/pnas.2110472118>, 2021.
- 1459 O'Dowd, C., Monahan, C., and Dall'Osto, M.: On the occurrence of open ocean particle production and growth events,  
 1460 *Geophys. Res. Lett.*, 37, 2010GL044679, <https://doi.org/10.1029/2010GL044679>, 2010.
- 1461 O'Dowd, C. D., Hämeri, K., Mäkelä, J., Väkeva, M., Aalto, P., de Leeuw, G., Kunz, G. J., Becker, E., Hansson, H.,  
 1462 Allen, A. G., Harrison, R. M., Berresheim, H., Kleefeld, C., Geever, M., Jennings, S. G., and Kulmala, M.: Coastal  
 1463 new particle formation: Environmental conditions and aerosol physicochemical characteristics during nucleation  
 1464 bursts, *J. Geophys. Res. Atmospheres*, 107, <https://doi.org/10.1029/2000JD000206>, 2002.
- 1465 Olfert, J. S., Kulkarni, P., and Wang, J.: Measuring aerosol size distributions with the fast integrated mobility  
 1466 spectrometer, *J. Aerosol Sci.*, 39, 940–956, <https://doi.org/10.1016/j.jaerosci.2008.06.005>, 2008.
- 1467 Pekour, M. and Ermold, B.: ARM Aerial Facility (AAF) Merged aerosol size distribution,  
 1468 <https://doi.org/10.5439/1905541>, 2017.
- 1469 Petters, M. D., Snider, J. R., Stevens, B., Vali, G., Faloona, I., and Russell, L. M.: Accumulation mode aerosol, pockets  
 1470 of open cells, and particle nucleation in the remote subtropical Pacific marine boundary layer, *J. Geophys. Res.*  
 1471 *Atmospheres*, 111, 2004JD005694, <https://doi.org/10.1029/2004JD005694>, 2006.
- 1472 Pirjola, L., O'Dowd, C. D., Brooks, I. M., and Kulmala, M.: Can new particle formation occur in the clean marine  
 1473 boundary layer?, *J. Geophys. Res. Atmospheres*, 105, 26531–26546, <https://doi.org/10.1029/2000JD900310>, 2000.
- 1474 Pope, S. B.: *Turbulent Flows*, 1st ed., Cambridge University Press, <https://doi.org/10.1017/CBO9780511840531>,  
 1475 2000.
- 1476 Pryor, S. C., Larsen, S. E., Sørensen, L. L., Barthelme, R. J., Grönholm, T., Kulmala, M., Launiainen, S., Rannik, Ü.,  
 1477 and Vesala, T.: Particle fluxes over forests: Analyses of flux methods and functional dependencies, *J. Geophys. Res.*,  
 1478 112, D07205, <https://doi.org/10.1029/2006JD008066>, 2007.
- 1479 Quinn, P. K., Coffman, D. J., Johnson, J. E., Upchurch, L. M., and Bates, T. S.: Small fraction of marine cloud  
 1480 condensation nuclei made up of sea spray aerosol, *Nat. Geosci.*, 10, 674–679, <https://doi.org/10.1038/ngeo3003>, 2017.
- 1481 Rannik, Ü. and Vesala, T.: Autoregressive filtering versus linear detrending in estimation of fluxes by the eddy  
 1482 covariance method, *Bound.-Layer Meteorol.*, 91, 259–280, <https://doi.org/10.1023/A:1001840416858>, 1999.
- 1483 Sakai, R. K., Fitzjarrald, D. R., and Moore, K. E.: Importance of Low-Frequency Contributions to Eddy Fluxes  
 1484 Observed over Rough Surfaces, *J. Appl. Meteorol.*, 40, 2178–2192, [https://doi.org/10.1175/1520-0450\(2001\)040<2178:IOLFCT>2.0.CO;2](https://doi.org/10.1175/1520-0450(2001)040<2178:IOLFCT>2.0.CO;2), 2001.
- 1486 Sanchez, K. J., Zhang, B., Liu, H., Saliba, G., Chen, C.-L., Lewis, S. L., Russell, L. M., Shook, M. A., Crosbie, E. C.,  
 1487 Ziemba, L. D., Brown, M. D., Shingler, T. J., Robinson, C. E., Wiggins, E. B., Thornhill, K. L., Winstead, E. L.,  
 1488 Jordan, C., Quinn, P. K., Bates, T. S., Porter, J., Bell, T. G., Saltzman, E. S., Behrenfeld, M. J., and Moore, R. H.:  
 1489 Linking marine phytoplankton emissions, meteorological processes, and downwind particle properties with  
 1490 FLEXPART, *Atmospheric Chem. Phys.*, 21, 831–851, <https://doi.org/10.5194/acp-21-831-2021>, 2021.
- 1491 Schaller, C., Göckede, M., and Foken, T.: Flux calculation of short turbulent events – comparison of three methods,  
 1492 *Atmospheric Meas. Tech.*, 10, 869–880, <https://doi.org/10.5194/amt-10-869-2017>, 2017.

1493 Schmid, B., Tomlinson, J. M., Hubbe, J. M., Comstock, J. M., Mei, F., Chand, D., Pekour, M. S., Kluzek, C. D.,  
1494 Andrews, E., Biraud, S. C., and McFarquhar, G. M.: The DOE ARM Aerial Facility, *Bull. Am. Meteorol. Soc.*, 95,  
1495 723–742, <https://doi.org/10.1175/BAMS-D-13-00040.1>, 2014.

1496 Siebert, H., Szodry, K.-E., Egerer, U., Wehner, B., Henning, S., Chevalier, K., Lücknerath, J., Welz, O., Weinhold, K.,  
1497 Lauermaun, F., Gottschalk, M., Ehrlich, A., Wendisch, M., Fialho, P., Roberts, G., Allwayin, N., Schum, S., Shaw,  
1498 R. A., Mazzoleni, C., Mazzoleni, L., Nowak, J. L., Malinowski, S. P., Karpinska, K., Kumala, W., Czyzewska, D.,  
1499 Luke, E. P., Kollias, P., Wood, R., and Mellado, J. P.: Observations of Aerosol, Cloud, Turbulence, and Radiation  
1500 Properties at the Top of the Marine Boundary Layer over the Eastern North Atlantic Ocean: The ACORES Campaign,  
1501 *Bull. Am. Meteorol. Soc.*, 102, E123–E147, <https://doi.org/10.1175/BAMS-D-19-0191.1>, 2021.

1502 Spirig, C., Neftel, A., Ammann, C., Dommen, J., Grabmer, W., Thielmann, A., Schaub, A., Beauchamp, J., Wisthaler,  
1503 A., and Hansel, A.: Eddy covariance flux measurements of biogenic VOCs during ECHO 2003 using proton transfer  
1504 reaction mass spectrometry, *Atmospheric Chem. Phys.*, 5, 465–481, <https://doi.org/10.5194/acp-5-465-2005>, 2005.

1505 Stull, R. B. (Ed.): *An Introduction to Boundary Layer Meteorology*, Springer Netherlands, Dordrecht,  
1506 <https://doi.org/10.1007/978-94-009-3027-8>, 1988.

1507 Sun, Y., Jia, L., Chen, Q., and Zheng, C.: Optimizing Window Length for Turbulent Heat Flux Calculations from  
1508 Airborne Eddy Covariance Measurements under Near Neutral to Unstable Atmospheric Stability Conditions, *Remote  
1509 Sens.*, 10, 670, <https://doi.org/10.3390/rs10050670>, 2018.

1510 Torrence, C. and Compo, G. P.: *A Practical Guide to Wavelet Analysis.*, *Bull. Am. Meteorol. Soc.*, 79, 61–78,  
1511 [https://doi.org/10.1175/1520-0477\(1998\)079<0061:APGTWA>2.0.CO;2](https://doi.org/10.1175/1520-0477(1998)079<0061:APGTWA>2.0.CO;2), 1998.

1512 Wang, J., Pikridas, M., Spielman, S. R., and Pinterich, T.: A fast integrated mobility spectrometer for rapid  
1513 measurement of sub-micrometer aerosol size distribution, Part I: Design and model evaluation, *J. Aerosol Sci.*, 108,  
1514 44–55, <https://doi.org/10.1016/j.jaerosci.2017.02.012>, 2017a.

1515 Wang, J., Pikridas, M., Pinterich, T., Spielman, S. R., Tsang, T., McMahon, A., and Smith, S.: A Fast Integrated  
1516 Mobility Spectrometer for rapid measurement of sub-micrometer aerosol size distribution, Part II: Experimental  
1517 characterization, *J. Aerosol Sci.*, 113, 119–129, <https://doi.org/10.1016/j.jaerosci.2017.05.001>, 2017b.

1518 Wang, J., Wood, R., Jensen, M., Azevedo, E., Bretherton, C., and Chand, D.: *Aerosol and Cloud Experiments in  
1519 Eastern North Atlantic (ACE-ENA) Field Campaign Report*, 2019.

1520 Weber, R. J., Marti, J. J., McMurry, P. H., Eisele, F. L., Tanner, D. J., and Jefferson, A.: Measurements of new particle  
1521 formation and ultrafine particle growth rates at a clean continental site, *J. Geophys. Res. Atmospheres*, 102, 4375–  
1522 4385, <https://doi.org/10.1029/96JD03656>, 1997.

1523 Weber, R. J., Clarke, A. D., Litchy, M., Li, J., Kok, G., Schillawski, R. D., and McMurry, P. H.: Spurious aerosol  
1524 measurements when sampling from aircraft in the vicinity of clouds, *J. Geophys. Res. Atmospheres*, 103, 28337–  
1525 28346, <https://doi.org/10.1029/98JD02086>, 1998.

1526 Wiedensohler, A., Covert, D. S., Swietlicki, Erik., Aalto, Pasi., Heintzenberg, Jost., and Leck, C.: Occurrence of an  
1527 ultrafine particle mode less than 20 nm in diameter in the marine boundary layer during Arctic summer and autumn,  
1528 *Tellus B*, 48, 213–222, <https://doi.org/10.1034/j.1600-0889.1996.t01-1-00006.x>, 1996.

1529 Wolfe, G. M., Kawa, S. R., Hanisco, T. F., Hannun, R. A., Newman, P. A., Swanson, A., Bailey, S., Barrick, J.,  
1530 Thornhill, K. L., Diskin, G., DiGangi, J., Nowak, J. B., Sorenson, C., Bland, G., Yungel, J. K., and Swenson, C. A.:  
1531 The NASA Carbon Airborne Flux Experiment (CARAFE): instrumentation and methodology, *Atmospheric Meas.  
1532 Tech.*, 11, 1757–1776, <https://doi.org/10.5194/amt-11-1757-2018>, 2018.

- 1533 Wood, R. and Bretherton, C. S.: Boundary Layer Depth, Entrainment, and Decoupling in the Cloud-Capped  
1534 Subtropical and Tropical Marine Boundary Layer, *J. Clim.*, 17, 3576–3588, [https://doi.org/10.1175/1520-0442\(2004\)017<3576:BLDEAD>2.0.CO;2](https://doi.org/10.1175/1520-0442(2004)017<3576:BLDEAD>2.0.CO;2), 2004.
- 1536 Wood, R., Wyant, M., Bretherton, C. S., Rémillard, J., Kollias, P., Fletcher, J., Stemmler, J., de Szoeko, S., Yuter, S.,  
1537 Miller, M., Mechem, D., Tselioudis, G., Chiu, J. C., Mann, J. A. L., O'Connor, E. J., Hogan, R. J., Dong, X., Miller,  
1538 M., Ghate, V., Jefferson, A., Min, Q., Minnis, P., Palikonda, R., Albrecht, B., Luke, E., Hannay, C., and Lin, Y.:  
1539 Clouds, Aerosols, and Precipitation in the Marine Boundary Layer: An Arm Mobile Facility Deployment, *Bull. Am. Meteorol. Soc.*, 96, 419–440, <https://doi.org/10.1175/BAMS-D-13-00180.1>, 2015.
- 1541 Wulfmeyer, V., Muppa, S. K., Behrendt, A., Hammann, E., Späth, F., Sorbjan, Z., Turner, D. D., and Hardesty, R.  
1542 M.: Determination of Convective Boundary Layer Entrainment Fluxes, Dissipation Rates, and the Molecular  
1543 Destruction of Variances: Theoretical Description and a Strategy for Its Confirmation with a Novel Lidar System  
1544 Synergy, *J. Atmospheric Sci.*, 73, 667–692, <https://doi.org/10.1175/JAS-D-14-0392.1>, 2016.
- 1545 Yoon, Y. J. and Brimblecombe, P.: Modelling the contribution of sea salt and dimethyl sulfide derived aerosol to  
1546 marine CCN, *Atmospheric Chem. Phys.*, 2, 17–30, <https://doi.org/10.5194/acp-2-17-2002>, 2002.
- 1547 Zhang, J., Chen, Y.-S., Yamaguchi, T., and Feingold, G.: Cloud water adjustments to aerosol perturbations are  
1548 buffered by solar heating in non-precipitating marine stratocumuli, *Atmospheric Chem. Phys.*, 24, 10425–10440,  
1549 <https://doi.org/10.5194/acp-24-10425-2024>, 2024.
- 1550 Zheng, G., Wang, Y., Aiken, A. C., Gallo, F., Jensen, M. P., Kollias, P., Kuang, C., Luke, E., Springston, S., Uin, J.,  
1551 Wood, R., and Wang, J.: Marine boundary layer aerosol in the eastern North Atlantic: seasonal variations and key  
1552 controlling processes, *Atmospheric Chem. Phys.*, 18, 17615–17635, <https://doi.org/10.5194/acp-18-17615-2018>,  
1553 2018.
- 1554 Zheng, G., Wang, Y., Wood, R., Jensen, M. P., Kuang, C., McCoy, I. L., Matthews, A., Mei, F., Tomlinson, J. M.,  
1555 Shilling, J. E., Zawadowicz, M. A., Crosbie, E., Moore, R., Ziemba, L., Andreae, M. O., and Wang, J.: New particle  
1556 formation in the remote marine boundary layer, *Nat. Commun.*, 12, 527, <https://doi.org/10.1038/s41467-020-20773-1>,  
1557 2021.

1558

▼  
▲  
**Page 6: [1] Deleted** Ajmal Rasheeda Satheesh 5/15/26 9:08:00 PM

▼  
▲  
**Page 20: [2] Deleted** Ajmal Rasheeda Satheesh 5/16/26 12:04:00 AM

▼  
▲  
**Page 20: [3] Formatted** Ajmal Rasheeda Satheesh 4/28/26 8:27:00 PM

Font color: Blue

▼  
▲  
**Page 20: [3] Formatted** Ajmal Rasheeda Satheesh 4/28/26 8:27:00 PM

Font color: Blue

▼  
▲  
**Page 20: [4] Deleted** Ajmal Rasheeda Satheesh 5/13/26 10:20:00 AM

▼  
▲  
**Page 20: [4] Deleted** Ajmal Rasheeda Satheesh 5/13/26 10:20:00 AM

▼  
▲  
**Page 20: [4] Deleted** Ajmal Rasheeda Satheesh 5/13/26 10:20:00 AM

▼  
▲  
**Page 20: [4] Deleted** Ajmal Rasheeda Satheesh 5/13/26 10:20:00 AM

▼  
▲  
**Page 20: [4] Deleted** Ajmal Rasheeda Satheesh 5/13/26 10:20:00 AM

▼  
▲  
**Page 20: [5] Formatted** Ajmal Rasheeda Satheesh 4/28/26 8:27:00 PM

Font color: Blue

▼  
▲  
**Page 20: [5] Formatted** Ajmal Rasheeda Satheesh 4/28/26 8:27:00 PM

Font color: Blue

▼  
▲  
**Page 20: [5] Formatted** Ajmal Rasheeda Satheesh 4/28/26 8:27:00 PM

Font color: Blue

▼  
▲  
**Page 20: [5] Formatted** Ajmal Rasheeda Satheesh 4/28/26 8:27:00 PM

Font color: Blue

▼  
▲  
**Page 20: [5] Formatted** Ajmal Rasheeda Satheesh 4/28/26 8:27:00 PM

Font color: Blue

▼  
▲  
**Page 20: [5] Formatted** Ajmal Rasheeda Satheesh 4/28/26 8:27:00 PM

Font color: Blue

▲

**Page 20: [5] Formatted** **Ajmal Rasheeda Satheesh** **4/28/26 8:27:00 PM**

Font color: Blue

**Page 20: [5] Formatted** **Ajmal Rasheeda Satheesh** **4/28/26 8:27:00 PM**

Font color: Blue

**Page 20: [5] Formatted** **Ajmal Rasheeda Satheesh** **4/28/26 8:27:00 PM**

Font color: Blue

**Page 20: [5] Formatted** **Ajmal Rasheeda Satheesh** **4/28/26 8:27:00 PM**

Font color: Blue

**Page 20: [5] Formatted** **Ajmal Rasheeda Satheesh** **4/28/26 8:27:00 PM**

Font color: Blue

**Page 20: [5] Formatted** **Ajmal Rasheeda Satheesh** **4/28/26 8:27:00 PM**

Font color: Blue

**Page 20: [5] Formatted** **Ajmal Rasheeda Satheesh** **4/28/26 8:27:00 PM**

Font color: Blue

**Page 20: [5] Formatted** **Ajmal Rasheeda Satheesh** **4/28/26 8:27:00 PM**

Font color: Blue

**Page 20: [5] Formatted** **Ajmal Rasheeda Satheesh** **4/28/26 8:27:00 PM**

Font color: Blue

**Page 20: [5] Formatted** **Ajmal Rasheeda Satheesh** **4/28/26 8:27:00 PM**

Font color: Blue

**Page 20: [5] Formatted** **Ajmal Rasheeda Satheesh** **4/28/26 8:27:00 PM**

Font color: Blue

**Page 20: [5] Formatted** **Ajmal Rasheeda Satheesh** **4/28/26 8:27:00 PM**

Font color: Blue

**Page 20: [5] Formatted** **Ajmal Rasheeda Satheesh** **4/28/26 8:27:00 PM**

Font color: Blue

**Page 20: [5] Formatted** **Ajmal Rasheeda Satheesh** **4/28/26 8:27:00 PM**

Font color: Blue

**Page 20: [5] Formatted** **Ajmal Rasheeda Satheesh** **4/28/26 8:27:00 PM**

Font color: Blue

▲  
**Page 20: [5] Formatted**                      **Ajmal Rasheeda Satheesh**                      **4/28/26 8:27:00 PM**

Font color: Blue

▲  
**Page 20: [5] Formatted**                      **Ajmal Rasheeda Satheesh**                      **4/28/26 8:27:00 PM**

Font color: Blue

▲  
**Page 20: [5] Formatted**                      **Ajmal Rasheeda Satheesh**                      **4/28/26 8:27:00 PM**

Font color: Blue

▲  
**Page 20: [5] Formatted**                      **Ajmal Rasheeda Satheesh**                      **4/28/26 8:27:00 PM**

Font color: Blue

▲  
**Page 20: [5] Formatted**                      **Ajmal Rasheeda Satheesh**                      **4/28/26 8:27:00 PM**

Font color: Blue

▲  
**Page 20: [6] Deleted**                      **Ajmal Rasheeda Satheesh**                      **4/27/26 7:21:00 PM**

✖